Lewis Acid Strength of Interfacial Metal Sites Drives CH₃OH Selectivity and Formation Rates on Cu-based CO₂ Hydrogenation Catalysts

Gina Noh, Erwin Lam, Daniel T. Bregante, Jordan Meyet, Petr Šot, David W. Flaherty, Christophe Copéret*

Abstract: CH_3OH formation rates in CO_2 hydrogenation on Cu-based catalysts sensitively depend on the nature of the support and the presence of promoters. In this context, Cu nanoparticles supported on tailored supports decorated with highly dispersed M sites on SiO_2 (Cu/M@SiO_2; M = Ti, Zr, Hf, Nb, Ta) were prepared via Surface Organometallic Chemistry, and their catalytic performance (reactivity/selectivity) was systematically investigated for the hydrogenation of CO_2 to CH_3OH. The presence of Lewis acid sites enhances CH_3OH formation rates, while CO formation rates are unaffected. Measures of the Lewis acid strength and detection of methoxy reaction intermediates indicate that the promotion of CH_3OH formation rates and selectivities likely originate from the stabilization of formate and methoxy surface intermediates at the periphery of Cu nanoparticles. The stabilization of surface intermediates depends sensitively on the Lewis acid strength of M sites, determined by measuring enthalpies of pyridine adsorption and the ^{13}C chemical shifts of OCH_3 coordinated to M, which are demonstrated here to be a molecular descriptor for Lewis acidity and reactivity in CO_2 hydrogenation.

Table of Contents

Section S1: Experimental

General procedures

All manipulations for support preparation, organometallic synthesis, and organometallic grafting were performed under argon atmosphere in an MBRAUN UNIlab glove box or using standard Schlenk techniques. Toluene and pentane were dried by using a two-column solvent purification system (MBRAUN MB-SPS-800, equipped with MBRAUN SPS alumina columns), then stored over 4Å molecular sieve (activated by treatment under vacuum (~10^{-3} Pa) at 573 K for 12 h); tetrahydrofuran and C_6D_6 were distilled from Na^0/benzophenone under argon and under vacuum (~10^{-3} Pa), respectively, then stored over activated 4Å molecular sieve. Celite® was placed in a Schlenk frit, dried at 423 K for 12 h before being flame dried under vacuum. NH_4Cl (AlfaAesar, 99.999 %) was dried under vacuum (~10^{-1} Pa) at 323 K overnight before being transferred in a glovebox. Reagents were used as received unless otherwise specified. $[Cu(O^tBu)]_4$,[1] $Ti(OSi(O^tBu)_3)_3(O^iPr)$,[2] $Hf(OSi(O^tBu)_3)_4$,[3] $Zr(OSi(O^tBu)_3)_4$,[3] and $Nb(OSi(O^tBu)_3)_3(O^iPr)_2$,[4] were synthesized according to literature procedures. The syntheses of $[Nb(OCH_3)_5]_2$,[5] $[Ta(OCH_3)_5]_2$,[6] and $Ta(OSi(O^tBu)_3)_3(O^iPr)_2$[7] were adapted from literature procedures and are reported below; the products were verified via single crystal X-ray diffraction.

Solution ^{1}H and ^{13}C nuclear magnetic resonance (NMR) spectra (C_6D_6, 298 K) were recorded using a Bruker 300 MHz NMR spectrometer. ^{1}H NMR spectra analyzed for quantification used ferrocene as an internal standard and a relaxation delay (d1) of 60 s. [1]H chemical shifts were referenced to the residual solvent peak at 7.16 ppm. Solution ^{1}H and ^{13}C NMR spectra of the molecular compounds $[Nb(OCH_3)_5]_2$ and $[Ta(OCH_3)_5]_2$ were recorded on a Bruker 400 MHz AVANCE III spectrometer. The solution ^{1}H-^{13}C HSQC spectra were also recorded. The chemical shifts were referenced to the residual peak at 7.16 ppm (^{1}H) and 128.06 ppm (^{13}C). NMR spectra for $[Nb(OCH_3)_5]_2$ and $[Ta(OCH_3)_5]_2$ are included in Section S10.

Infrared (IR) spectra of the molecular compounds $[Nb(OCH_3)_5]_2$ and $[Ta(OCH_3)_5]_2$ were collected under inert atmosphere using a Bruker Alpha spectrometer in attenuated total reflectance (ATR) mode, equipped with a diamond ATR module (uncooled deuterated triglycine sulfate (DTGS) detector, 2 cm^{-1} spectral resolution, 400-4000 cm^{-1}, average of 32 scans; spectra included in Section S2). IR spectra of the catalyst solids were collected at each step of the synthesis under argon atmosphere. IR spectra of self-supporting wafers (0.01-0.02 g.cm^{-2}) were recorded in transmission mode using a Bruker Alpha FT-IR spectrometer (uncooled DTGS detector, 4 cm^{-1} spectral resolution, 400-4000 cm^{-1}, average of 24 scans; transmission module), unless stated otherwise. Spectra are normalized using the Si-O-Si overtones of the SiO_2 support for all SiO_2-containing materials.

Preparation of $[Nb(OCH_3)_5]_2$

To a red solution of 1.5 g of $NbCl_5$ (5.55 mmol, 1 equiv.) and 1.48 g of NH_4Cl (27.7 mmol, 5 equiv.) in toluene (20 ml) cooled to 273 K, was added dropwise 20 ml of dry CH_3OH. The solution immediately became colorless after addition of dry CH_3OH and was stirred for 2 h at 273 K. A toluene suspension of 1.08 g of $NaNH_2$ (27.7 mmol, 5 equiv.) was added dropwise to the cold mixture then stirred for 30 min at 273 K; the mixture was warmed to 298 K and stirred for an additional hour. The colorless solution, containing a white precipitate, was filtered over Celite®, and the solvent was removed in vacuo to yield a yellow oily residue. The residue was sublimed at 323 K (10^{-3} Pa). The desired material, $[Nb(OCH_3)_5]_2$, was recovered as a white solid (38% yield).

Spectra for this compound are included in the ESI, Section S10.
^{1}H NMR (C_6D_6, 300 MHz): δ 4.06 ppm (6 H, μ_2-OCH_3), 4.24 ppm (24 H, μ_1-OCH_3); ^{13}C NMR (C_6D_6, 300 MHz): δ 60.5 ppm (μ_2-OCH_3), 61.1 ppm (μ_1-OCH3); IR (Diamond ATR): 2915, 2888, 2816, 2801, 1451, 1430, 1150, 1061, 1018, 523, 471 cm^{-1}

Preparation of $[Ta(OCH_3)_5]_2$

To a yellow solution of 1.97 g of $TaCl_5$ (5.50 mmol, 1 equiv.) and 1.48 g of NH_4Cl (27.7 mmol, 5 equiv.) in toluene (20 ml) cooled to 273 K, was added dropwise 20 ml of dry CH_3OH. The solution immediately turned colorless after the addition of CH_3OH and was stirred for 1 h at 273 K. A toluene suspension of 1.08 g of $NaNH_2$ (27.7 mmol, 5 equiv.) was added dropwise to the cold mixture, which was then stirred for 30 min at 273 K. The solution was allowed to slowly warm to 298 K then stirred for 12 h at 298 K. The colorless solution, containing a white precipitate, was filtered over Celite®. The solvent

was removed in vacuo, leaving an off-white residue. The residue was sublimed (10^{-3} Pa) at 313 K. The desired material was recovered as a white solid (42% yield).

Spectra for this compound are included in the ESI, Section S10.

^{1}H NMR (C_6D_6, 300 MHz): δ 4.11 ppm (6 H, μ_2-OCH_3), 4.34 ppm (24 H, μ_1-OCH_3); ^{13}C NMR (C_6D_6, 300 MHz): δ 59.6 ppm (-OCH_3) ; IR (Diamond ATR): 2922, 2897, 2822, 2807, 1455, 1436, 1157, 1076, 1009, 566, 472 cm^{-1}

Preparation of Ta(OSi(O^{t}Bu)$_3$)$_3$(O^{i}Pr)$_2$

To a colorless solution of 0.5 g (0.74 mmol, 1 equiv.) of [Ta(OCH$_3$)$_5$]$_2$ in pentane (20 ml) was added 20 ml of dry C_3H_7OH. After stirring for 30 min. at 298 K, 1 g (3.7 mmol, 5 equiv.) Si(O^{t}Bu)$_3$OH in pentane (20 mL) was added dropwise. The solution was stirred for 1 h at 298 K. The solvent was removed in vacuo. The unreacted Si(O^{t}Bu)$_3$OH was removed by sublimation at 333 K (10^{-3} Pa). The product was redissolved in pentane. Concentration and cooling (238 K) of the solution afforded colorless crystals. The product was confirmed by H-NMR; the spectrum was consistent with previous reports.[7]

Catalyst synthesis

Fumed SiO_2 (Evonik AEROSIL 200) was formed into aggregates by combining with deionized distilled water (MilliQ; resistivity > 18.2 MΩ.cm) to form a thick slurry, drying at 393 K for >24 h, then crushing and sieving to retain aggregates 250-450 μm in size. The aggregates were treated at 973 K (0.0167 K.s^{-1}) for 12 h under flowing synthetic air (PanGas; 1.67 cm^3.s^{-1}) then cooled to room temperature under high vacuum (~10^{-3} Pa) to yield $SiO_{2\text{-}700}$. $SiO_{2\text{-}500}$ was prepared from compacted SiO_2 by treatment at 773 K (0.0167 K.s^{-1}) for 12 h under flow of synthetic air (1.67 cm^3.s^{-1}) followed by treatment under high vacuum (~10^{-3} Pa) while cooling to room temperature. The number of hydroxyl groups accessible for grafting for $SiO_{2\text{-}700}$ and $SiO_{2\text{-}500}$ was determined by reaction of [Mg(CH$_2$Ph)$_2$(THF)$_2$][8] with the oxide materials (in C_6D_6) and quantification of the released toluene using ^{1}H NMR; these values are 0.49 and 0.38 mmol OH.g^{-1} for $SiO_{2\text{-}500}$ and $SiO_{2\text{-}700}$, respectively (corresponding to areal densities of 1.5 and 1.1 OH.nm^{-2} SiO_2, respectively).

M-decorated SiO_2 supports (M@SiO_2, where M = Ti, Zr, Hf, or Nb) were prepared using the method as described next. A solution of the appropriate precursor (Ti(OSi(O^{t}Bu)$_3$)$_3$(O^{i}Pr), Hf(OSi(O^{t}Bu)$_3$)$_4$, Zr(OSi(O^{t}Bu)$_3$)$_4$, Nb(OSi(O^{t}Bu)$_3$)$_3$(O^{i}Pr)$_2$), or Ta(OSi(O^{t}Bu)$_3$)$_3$(O^{i}Pr)$_2$) in toluene (0.15 mmol; 20 mL) was added to a slurry of $SiO_{2\text{-}700}$ (1 g) in toluene (10 mL) then stirred for 12 h. The supernatant was decanted from the settled slurry. The material was rinsed three times with toluene then dried under vacuum (~10^{-3} Pa) at room temperature, followed by treatment under vacuum (~10^{-3} Pa) at 773 K (0.083 K.s^{-1}) for 5 h.

Cu nanoparticles were dispersed on M@SiO_2 and $SiO_{2\text{-}500}$ supports: a solution of [Cu(O^{t}Bu)]$_4$ in pentane (0.2 mmol; 20 mL) was added to a slurry of the support (1 g for M@SiO_2 or $SiO_{2\text{-}500}$) in pentane (10 mL) and stirred for 12 h. The solvent was decanted, and the solids were washed thoroughly with pentane three times. The solids were dried at 298 K (~10^{-3} Pa), treated under flowing H_2 (101 kPa, PanGas 99.999%) at 773 K (0.083 K.s^{-1}) for 5 h, then cooled to 298 K under flow of H_2.

Catalyst characterization

Transmission electron microscopy (TEM) images of samples exposed to ambient conditions were obtained using a Hitachi HT7700 microscope (100 kV; bright field detector). Samples were prepared for imaging by depositing samples as dry fine powders onto ultrathin lacey carbon on a 300 mesh Au grids (Ted Pella) then agitating to remove the excess powder. Micrographs were processed using ImageJ to obtain the particle size distribution by assessing >150 particles. The particle size distribution was fit to lognormal distributions.

The number of surface Cu atoms (Cu$_s$) was determined by titration using N_2O pulses (assuming a 2:1 Cu:N_2O stoichiometry; 363 K). The sample (30-50 mg) was placed in a quartz u-tube reactor (8 mm ID) on a plug of quartz wool, with a K-type thermocouple aligned axially with the center of the catalyst bed. The reactor was placed within the BELCAT-B apparatus (BEL Japan, Inc.) and treated under a flow of 50% H_2/He (PanGas 99.999%; 0.5 cm^3.s^{-1}) at 573 K for 2 h (14 K.min^{-1}) before cooling to analysis temperature. Pulses of N_2O (1% N_2O in He, PanGas; 2.6-2.8 μL$_{STP}$ N_2O per pulse) were introduced by an injection valve every 120 s. The N_2O and N_2 contents of the reactor effluent were monitored by thermal conductivity detection.

Cu, Ti, Zr, Hf, and Nb contents were determined by inductively coupled plasma – atomic emission spectroscopy (Mikroanalytisches Labor Pascher, Remagen, Germany).

IR spectra (Nicolet NEXUS 6700 infrared spectrometer; 2 cm^{-1} spectral resolution, 1200-4000 cm^{-1}, average of 64 scans) of catalysts exposed to CO (298 K) were collected in transmission mode using an uncooled deuterated tryglycine sulfate (DTGS) KBr detector. A wafer of catalyst material (0.01-0.02 g.cm^{-1}) was pressed into an aluminum ring, which was placed into a glass vacuum cell with CaF$_2$ windows. The cell was exposed to 3.5 Pa CO at 298 K for 5 min; an IR spectrum was collected with the material under CO atmosphere. The cell was then evacuated (~10^{-3} Pa) for 15 minutes at 298 K, then an IR spectrum was collected.

The presence and strength of Lewis acid sites in M@SiO$_2$ were characterized by the IR spectra of adsorbed pyridine using a custom-built transmission cell[9] coupled to a Fourier transform-infrared (FTIR) spectrometer (Bruker, Vertex 70) with a liquid N$_2$-cooled HgCdTe detector. Catalysts were pressed into self-supporting disks (~40 mg) and placed within the transmission cell, which was assembled using CaF$_2$ windows and connected to a gas manifold with lines heated to 423 K. All materials were first heated to 573 K at 10 K min^{-1} and held for 2 h under flowing He (70 cm^3 min^{-1}; Airgas, Ultra-zero grade), with the intent to desorb water and residual organics. Pyridine (0.1 kPa; Sigma-Aldrich, 99%) was introduced via a syringe pump (KD Scientific, Legato 100) and vaporized in the heated gas-transfer lines into a stream of flowing He (70 cm^3 min^{-1}). Steady-state IR spectra (128 scans, 1 cm^{-1} resolution) were obtained as a function of temperature (453 – 523 K) while flowing the pyridine/He stream over the samples.

Ex situ nuclear magnetic resonance (NMR) experiments were performed to examine the surface intermediates present on the catalyst materials. Samples (100 mg) were contacted with 5 bar of ^{13}CO$_2$ and H$_2$ (in 1:3 ratio) in a thick-walled glass reactor for 12 h at 503 K and subsequently cooled rapidly to 77 K. The material was treated under vacuum at 298 K (10^{-3} Pa) for 0.5 h. The treated material was loaded into a 4 mm rotor for solid-state NMR in an argon atmosphere glove box without exposure to atmosphere. Solid-state NMR spectra (^{1}H and ^{13}C) were recorded on a Bruker 400 MHz AVANCE III HD spectrometer equipped with a 4 mm magic-angle-spinning (MAS) triple resonance probe operating in double resonance mode with a MAS frequency of 10 kHz. Ramped cross-polarization (^{1}H-^{13}C) with ^{1}H excitation frequency of 100 kHz was used for most experiments. The contact time was maintained at 2 ms. Adamantane was used as an external secondary reference to calibrate chemical shifts.

X-Ray absorption spectroscopy

X-Ray absorption spectra at the Nb K-edge, Hf L-edges, or Ta L-edges were measured at the SuperXAS beamline at the Swiss Light Source (SLS). The SLS operates in top-up mode at a 2.4 GeV electron energy and a current of 400 mA. The incident photon beam provided by a 2.9 T super bend magnet source was selected by a Si(111) quick-EXAFS monochromator.[10] Focusing and the rejection of higher harmonics were achieved using a rhodium-coated collimating mirror at 2.5 mrad. During the measurements, the monochromator rotated with 10 Hz frequency, and X-ray absorption spectra were collected in transmission mode using ionization chambers developed for quick data collection with 1 MHz frequency.[10] The resulting spectra were averaged over 5 minutes using ProXAS software.[11] Calibration of the monochromator energy position was performed by setting the inflection point of a Pt foil spectrum recorded simultaneous with the samples (set to 11564 eV) for Hf and Ta. The calibration for the Nb K-edge was performed using a Nb foil, setting the inflection point at 18956 eV.

Ex situ samples were pressed in pellets of optimal thickness for transmission detection. Pellets were prepared in an Ar-filled glovebox and sealed within two aluminized plastic bags (polyaniline (14 µm), polyethylene (15 µm), Al (12 µm), polyethylene (75 µm); Gruber-Folien GmbH & Co. KG) using an impulse heat sealer to avoid exposure to air. One bag was removed immediately before measurement.

EXAFS data were analyzed using Demeter software package (version 0.9.26).[12] The data were fitted in R-space, after a Fourier Transform, using a k-weight of 3 and a window based on a Hanning function with dR = 0.5 and dk = 1. The specific ranges and values are specified below every spectrum. In the case of highly intense glitches, the k-range was adjusted to exclude them from Fourier Transform; glitches at k < 13 were removed manually. The respective scattering paths were generated based on available crystallographic data (Hf) or DFT-derived geometry-optimized models (Ta, Nb). The parameters R, σ, and ΔE were optimized during the fitting procedure, while the parameter *N* was fixed. The value of S$_0^2$ was obtained from fitting the molecular compounds. The amount of fitted parameters was below the 2/3 of the Nyquist criterion.

CO$_2$ hydrogenation reactions

Rates of CO$_2$ hydrogenation were measured at 503 K at differential reactant conversions (< 7%) on all samples (0.20-0.25 g), diluted with 5 g SiC (Fisher Scientific) and held against a sintered metal frit, axially centered within a tubular reactor (316 S.S., 9.1 mm i.d.) with plug-flow hydrodynamics. Temperatures were measured with a K-type thermocouple held at the mid-point of the packed bed and maintained using a resistively heated furnace with electronic controllers. Samples were treated at 573 K (0.083 K.s^{-1}) in H$_2$ flow (1 cm^3.s^{-1}; PanGas 99.999% H$_2$) for 1 h before cooling to reaction temperatures. CO$_2$, H$_2$, and Ar (CarbaGas; mixed in a 1:3:1 CO$_2$:H$_2$:Ar molar ratio) were introduced using electronic mass flow controllers (Bronkhorst EL-FLOW); total flow rates were varied between 6 and 100 cm^3.min^{-1} to vary reactant residence time without changes in individual reactant pressures. Transfer lines were heated (>393 K) to prevent product condensation. Reactor pressure was maintained at 2.6 MPa using a back-pressure regulator (Bronkhorst EL-PRESS). Reactant and product concentrations in the reactor effluent were measured using an on-line gas chromatograph (Agilent 7890N GC) equipped with Restek Rt-U-BOND (30 m x 0.53 mm x 20 μm) and Rt-Msieve 5A (30 m x 0.53 mm x 50 μm) columns, flame ionization detection (for CH$_3$OH and dimethylether), and thermal conductivity detection (for CO$_2$, H$_2$, Ar, and CO). Products measured were primarily CO and CH$_3$OH. Trace amounts of dimethylether (<0.005 selectivity), the bimolecular dehydration product of CH$_3$OH, were detected for Cu/Ti@SiO$_2$ and are accounted for in CH$_3$OH rates and selectivities (assuming 2:1 CH$_3$OH:dimethylether). Methane concentrations were below detection limits at all conditions on all samples.

Reaction rates for SiO$_2$ and M@SiO$_2$ materials were negligible (all product concentrations were below detection limits). Rates and selectivities for physically mixed Cu/SiO$_2$ and M@SiO$_2$ (1:1 mass ratio) were the same as for Cu/SiO$_2$ alone. Rates are calculated on a per-carbon basis and are normalized by the mass of Cu in each catalyst. Product selectivity is defined on a per-C basis. Negligible catalyst deactivation (<5% decrease in rates after 48 h) was detected by periodically measuring rates at a reference condition.

CH$_3$OH formation rates decreased as a function of increasing residence time for all samples except Cu/SiO$_2$. The rigorous extrapolation of rates to zero residence times to obtain initial rates requires knowledge of the functional form of the rate expression; in its absence, rates at the shortest residence times, where product inhibition is the least severe because of the low partial pressures of products at small reactant conversions, were extrapolated exponentially to obtain initial values. CO formation rates are nearly independent of residence time; their averaged values were taken as initial CO formation rates.

Section S2: Infrared spectra during catalyst synthesis
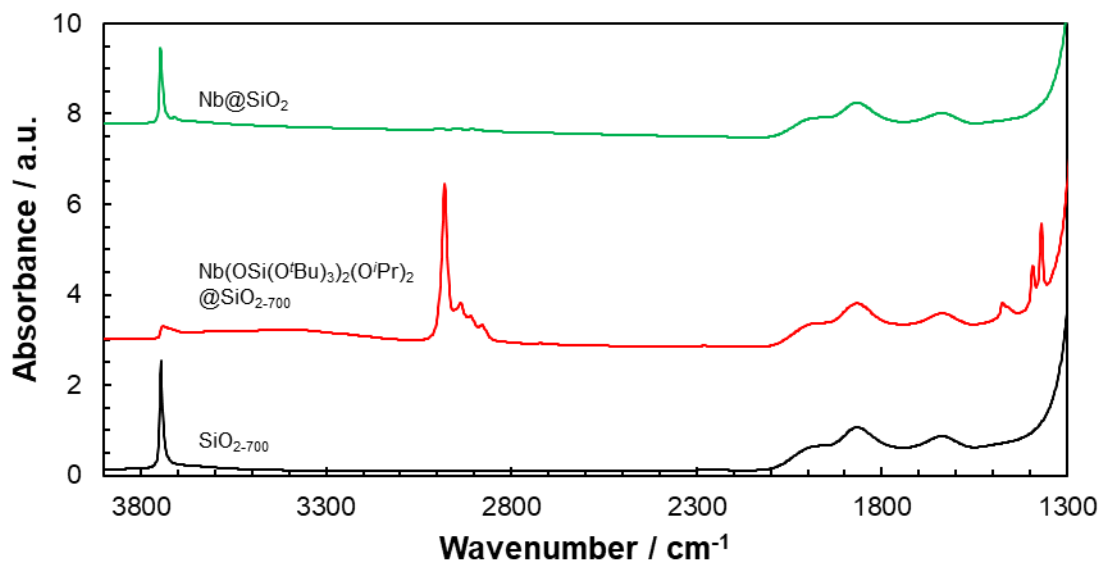
Figure S1a. Infrared spectra of solids during synthesis of Nb single sites on SiO_2 (Nb@SiO_2). SiO_{2-700} (bottom), after grafting of $Nb(OSi(O^tBu)_3)_3(O^iPr)_2$ on SiO_2 and rinsing and drying (middle), and after thermal treatment under vacuum (top).

Figure S1b. Infrared spectra of solids during synthesis of Cu nanoparticles on Nb@SiO_2 (Cu/Nb@SiO_2). Nb@SiO_2 (bottom), after grafting of $[Cu(O^tBu)]_4$ on Nb@SiO_2 and rinsing and drying (middle), and after thermal treatment under H_2 flow (top).
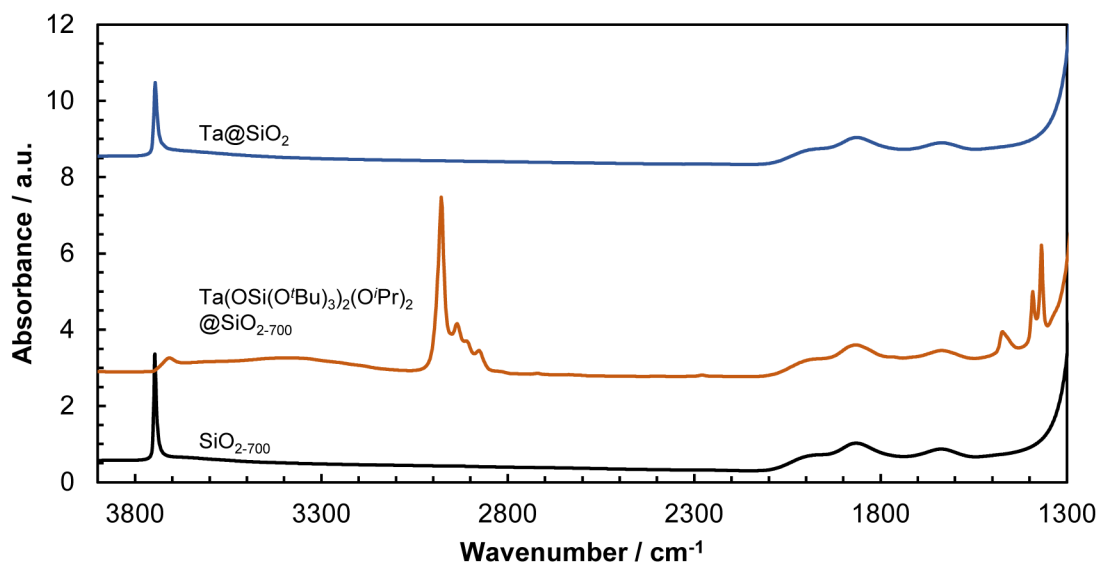
Figure S2a. Infrared spectra of solids during synthesis of Ta single sites on SiO_2 (Ta@SiO_2). SiO_{2-700} (bottom), after grafting of Ta(OSi(O^{t}Bu)$_3$)$_3$(O^{i}Pr)$_2$ on SiO_2 and rinsing and drying (middle), and after thermal treatment under vacuum (top).
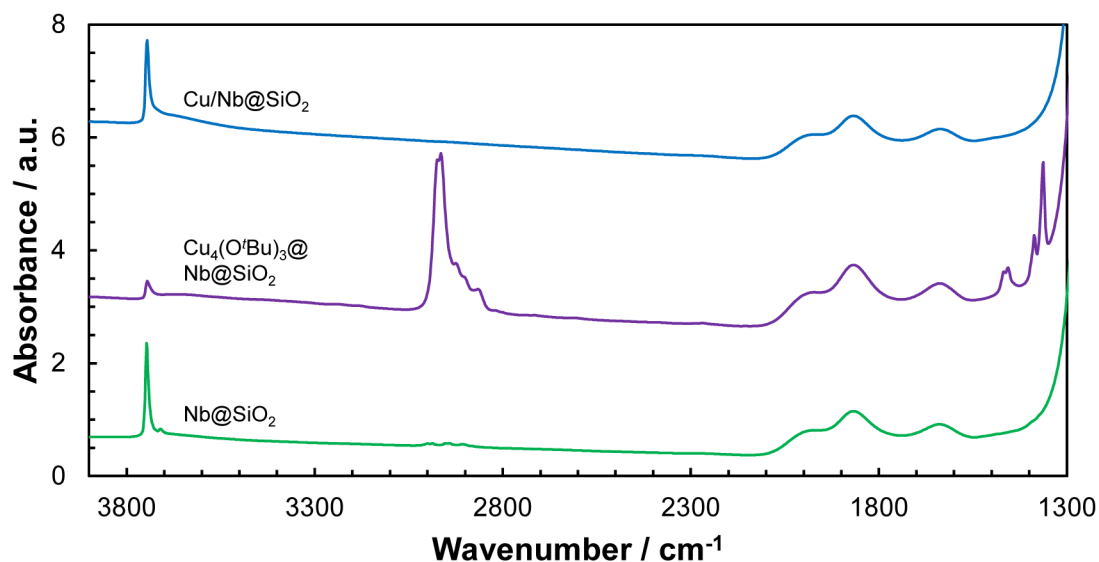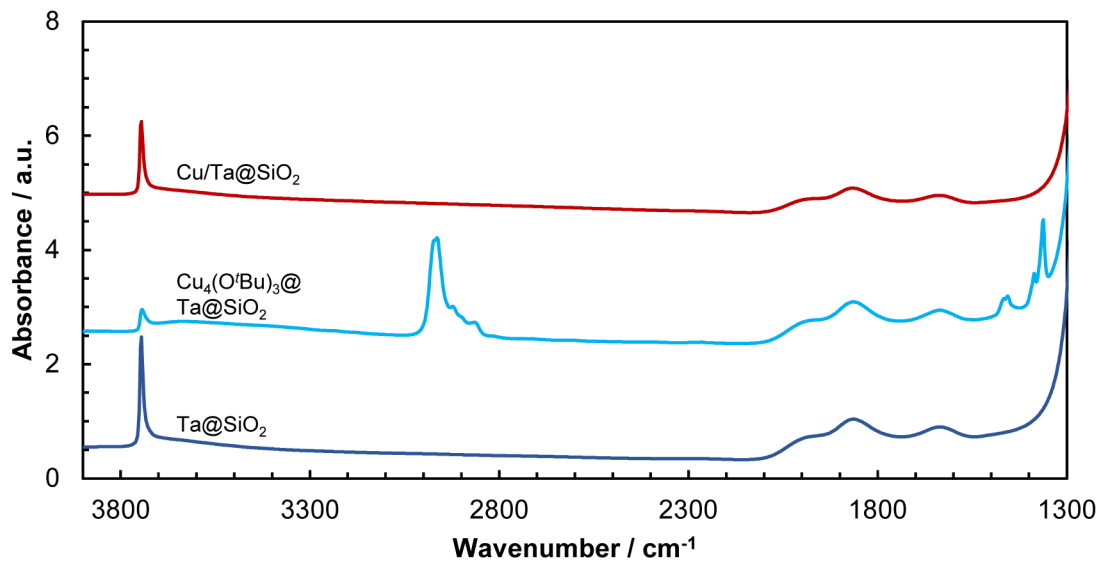

Figure S2b. Infrared spectra of solids during synthesis of Cu nanoparticles on Ta@SiO_2 (Cu/Ta@SiO_2). Ta@SiO_2 (bottom), after grafting of [Cu(O^{t}Bu)]$_4$ on Ta@SiO_2 and rinsing and drying (middle), and after thermal treatment under H_2 flow (top).

Section S3: Particle size distributions and sample micrographs

Cu/Nb@SiO$_2$

2.7 ± 0.6 nm
n = 150
μ = 1.04
σ^2 = 0.03

Cu/Ta@SiO$_2$

3.2 ± 0.5 nm
n = 150
μ = 1.15
σ^2 = 0.05
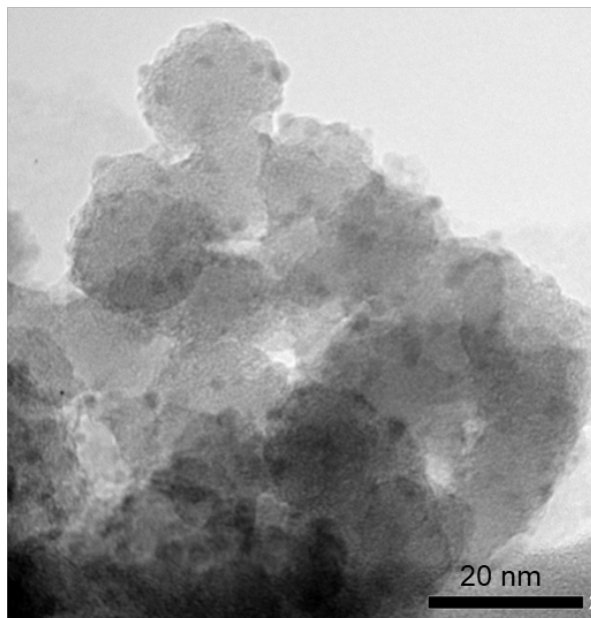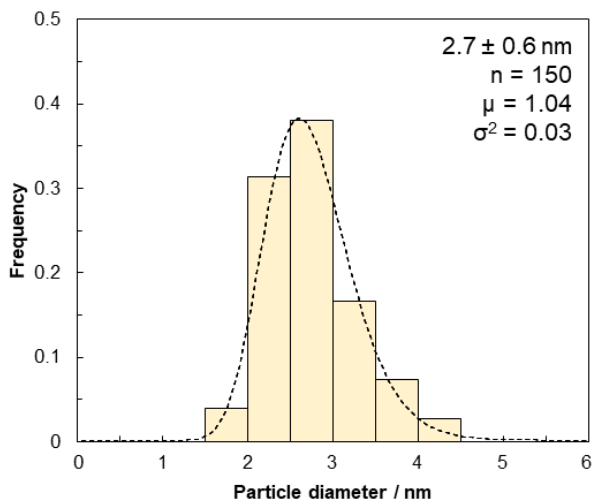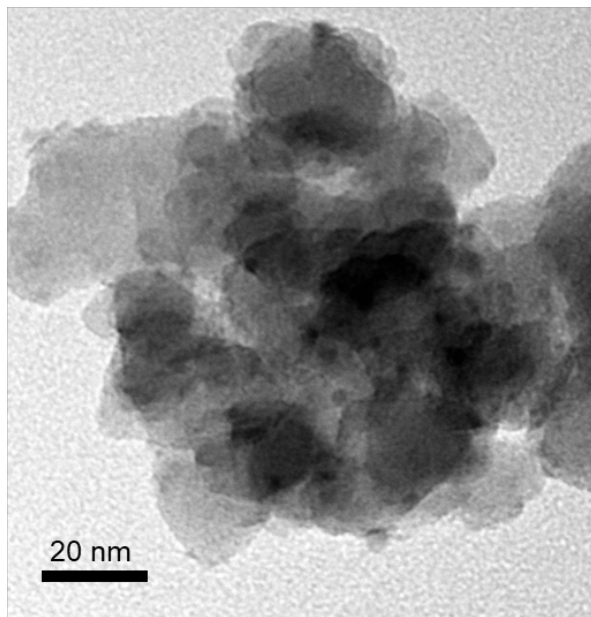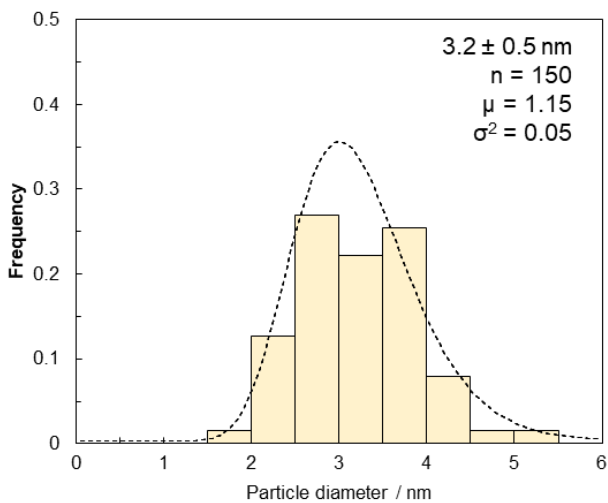
Figure S3. Cu particle size distribution and sample micrographs for Cu/Nb@SiO$_2$ (top) and Cu/Ta@SiO$_2$ (bottom). Number of particles (n) and fitting parameters (μ and σ^2) for the log-normal distributions are reported, inset in the plots.

Section S4: X-Ray absorption spectroscopy (XAS): near edge structure (XANES) and fine structure (EXAFS) spectra, fits, and analysis

In order to assess the isolation and the oxidation state of M (M = Hf, Ta, and Nb), XAS spectra were collected for as-synthesized M@SiO$_2$ and Cu/M@SiO$_2$ materials (without exposure to air), as well as for Cu/M@SiO$_2$ after catalytic testing ("spent", without exposure to air). Reference spectra (molecular precursors; Ta and Nb foils) were also recorded.

Normalized X-ray absorption near edge structure (XANES) spectra at the Nb K-edge are shown in Figure S4a for Nb@SiO$_2$, Cu/Nb@SiO$_2$, and Cu/Nb@SiO$_2$ after reaction (spent). Spectra for the Nb molecular precursor, Nb(O^{i}Pr)$_2$(OSi(O^{t}Bu)$_3$)$_3$, and a Nb foil are also shown. The first and second derivatives of the normalized absorbance are shown in Figures S4b and SX1c, respectively. The edge energy (E$_0$) is a sensitive indicator of oxidation state,[1] and its position is indicated by an inflection point (denoted in Figures S4b and S4c). This value (19003 eV) is nearly identical for Nb(O^{i}Pr)$_2$(OSi(O^{t}Bu)$_3$)$_3$, Nb@SiO$_2$, Cu/Nb@SiO$_2$, and Cu/Nb@SiO$_2$ (spent), indicating that the Nb oxidation state is the same among these materials (Nb(V)). In contrast, the Nb foil has a lower E$_0$ value (18986 eV).[2] The pre-edge features (indicated by the inflection point at 18990 eV in Figures S4b and S4c) for Nb(O^{i}Pr)$_2$(OSi(O^{t}Bu)$_3$)$_3$, Nb@SiO$_2$, Cu/Nb@SiO$_2$, and Cu/Nb@SiO$_2$ (spent) arise from 1s -> 4d electronic transitions and are only observable when p and d orbitals are hybridized.[1] Thus, increased centrosymmetry of the ligand field at the metal center (e.g., for O$_h$, compared to T$_d$) leads to a decrease in the intensity of this pre-edge feature. The intensity of the pre-edge increases from the molecular precursor to Nb@SiO$_2$ and further to Cu/Nb@SiO$_2$, likely reflecting the undercoordinated state of Nb in these materials (relative to the molecular precursor; the structure of Nb(O^{i}Pr)$_2$(OSi(O^{t}Bu)$_3$)$_3$ from force-field geometry optimizations has a nearly O$_h$ geometry, similar to the crystal structure reported for Ta(OEt)$_2$(OSi(O^{t}Bu)$_3$)$_3$[7]). The intensity of the pre-edge decreases significantly from the fresh Cu/Nb@SiO$_2$ material to the spent catalyst, reflecting the adsorption of surface species (methoxy, formate, H$_2$O) to these metal centers, concomitantly increasing the symmetry of their ligand fields.

To examine the well-dispersed nature of Nb metal centers, the extended X-ray absorption fine-structure (EXAFS) spectra were analyzed (Fig. S4d). Nb K-edge EXAFS spectra are shown in Figure S4d and were fit to obtain coordination numbers and the first and second coordination sphere. Tables S1-S4 show the fitting parameters for the Nb-containing materials. In no cases were Nb-Nb or Nb-O-Nb scattering paths able to be fit, with attempts to fit these spectra with Nb-Nb or Nb-O-Nb paths leading to extremely low degeneracy or high Debye-Waller factors, indicating that the presence of aggregated Nb is unlikely. Furthermore, the very low intensity of distant shells for all Nb@SiO$_2$ materials indicates that these cannot be attributed to Nb-Nb or Nb-O-Nb scattering paths. Together, these data indicate that Nb metal centers remain highly dispersed in Nb@SiO$_2$, Cu/Nb@SiO$_2$, and Cu/Nb@SiO$_2$ (spent). Additionally, Nb-Cu (and related) paths could not be fit for both Cu/Nb@SiO$_2$ and Cu/Nb@SiO$_2$ (spent). It is feasible that distant shells could arise from Cu scattering from proximal Cu nanoparticles, which is challenging to ascertain because of the absence of appropriate reference spectra. Nevertheless, these EXAFS fits, together with the overall similarity of XANES spectra among Nb@SiO$_2$, Cu/Nb@SiO$_2$, and Cu/Nb@SiO$_2$ (spent), indicate that Cu-Nb alloys are not formed and that for all materials, Nb is well-dispersed and retains a +5 oxidation state.

Similar trends in oxidation state (L$_1$-edge XANES) and site isolation (L$_3$-edge EXAFS) are observed for Ta and Hf. The normalized XANES spectra at the Ta L$_1$-edge is shown in Figure S5a for Ta(O^{i}Pr)$_2$(OSi(O^{t}Bu)$_3$)$_3$, Ta@SiO$_2$, Cu/Ta@SiO$_2$, and Cu/Ta@SiO$_2$ (spent), as well as for a Ta foil reference. The first and second derivatives of the normalized absorbance for the same materials are shown in Figures S5b and S5c, respectively. The edge energies for Ta(O^{i}Pr)$_2$(OSi(O^{t}Bu)$_3$)$_3$, Ta@SiO$_2$, Cu/Ta@SiO$_2$, and Cu/Ta@SiO$_2$ (spent) are nearly identical (11699 eV) and greater than that for the Ta foil (11684 eV), indicating that for all of these materials, Ta is in the same oxidation state (Ta(V)). For 5d metals, the pre-edge of the L$_1$-edge reflects 2s -> 5d electronic transitions and thus can be interpreted analogously to the pre-edge of the K-edge for 4d metals[1] (vide supra for Nb K-edge). The intensity of the pre-edge feature, indicated by the inflection point at 11686 eV in Figures S5b and S5c, increases from Ta(O^{i}Pr)$_2$(OSi(O^{t}Bu)$_3$)$_3$ to Ta@SiO$_2$ and to Cu/Ta@SiO$_2$, before decreasing in intensity for Cu/Ta@SiO$_2$ (spent). These trends are the same as those observed for the Nb pre-edge and indicate the decrease in the centrosymmetry of the Ta metal center from the molecular precursor (which is nearly O$_h$ in geometry, according to force-field geometry optimizations of a structure derived from the Ta(OEt)$_2$(OSi(O^{t}Bu)$_3$)$_3$ crystal structure[7]) to the isolated metal center on SiO$_2$ (in Ta@SiO$_2$ and in Cu/Ta@SiO$_2$). The pre-edge intensity decreases for the spent catalyst because of the adsorption of surface methoxy or formate species (or H$_2$O) onto Ta metal centers, increasing the symmetry of their ligand fields.

EXAFS fits and parameters for the Ta-containing materials (Ta L$_3$-edge) are shown in Figure S5d and Tables SX5-SX8, respectively. In all cases, Ta metal centers were determined to be well-dispersed. Scattering paths for Ta-Ta or Ta-O-Ta were not able to be fit for any material. Additionally, the very low intensity of distant shells for all Ta@SiO$_2$ materials indicate

that these cannot be attributed to scattering from distant Ta. It is possible that these distant shells arise from scattering by Cu, which has a much smaller atomic number than Ta. Together with XANES, these data indicate that Ta metal centers remain highly dispersed Ta(V) in Ta@SiO$_2$, Cu/Ta@SiO$_2$, and Cu/Ta@SiO$_2$ (spent).

The normalized XANES spectra at the Hf L$_1$-edge is shown in Figure S6a for Hf(OSi(O^{t}Bu)$_3$)$_4$, Hf@SiO$_2$, Cu/Hf@SiO$_2$, and Cu/Hf@SiO$_2$ (spent); the first and second derivatives of the normalized absorbance for the same materials are shown in Figures S6b and S6c, respectively. The edge energy for all Hf-containing materials is nearly identical (11284 eV), and greater than the reported value for the Hf metal (11270 eV), indicating that Hf is in a +4 oxidation state for all of these materials. The intensity of the pre-edge feature (at 11273 eV) is most pronounced for Hf(OSi(O^{t}Bu)$_3$)$_4$, consistent with its reported crystal structure[3] that is composed of a 1:1 mixture of Hf with four equivalent OSi(O^{t}Bu)$_3$ ligands and Hf with three equivalent ligands and one bi-dentate (κ^2) OSi(O^{t}Bu)$_3$ ligand. The intensity of the pre-edge decreases from the molecular precursor to Hf@SiO$_2$, Cu/Hf@SiO$_2$, and Cu/Hf@SiO$_2$ (spent), respectively. These changes indicate the increase of the centrosymmetry of the ligand field at the Hf metal center from the molecular precursor to all of the SiO$_2$-supported materials. The spent Cu/Hf@SiO$_2$ material has only a subtle pre-edge feature, reflecting the coordination of surface methoxy and formate species (or H$_2$O).

The EXAFS spectra at the Hf L$_3$-edge are shown in Figure S6d, with fits and parameters in Tables S9-S12. Similar to the EXAFS analysis for Nb and Ta, the Hf L$_3$-edge EXAFS indicates that Hf metal centers are well-dispersed. Hf-Hf and Hf-O-Hf scattering paths could not be adequately fit for any of these materials; attempts to fit these spectra with Hf-Hf and Hf-O-Hf paths led either to extremely low degeneracies or high Debye-Waller factors, indicating that the presence of aggregated Hf is unlikely. Thus, the very low intensity of distant shells for all SiO$_2$-supported materials renders these unlikely to arise from scattering by distant Hf metal centers but possibly from scattering by light elements (e.g., Cu). Taken together with the information from the XANES spectra, these trends indicate that Hf metal centers are highly dispersed Hf(IV) in Hf@SiO$_2$, Cu/Hf@SiO$_2$, and Cu/Hf@SiO$_2$ (spent).

Figure S4. (a) Normalized XANES spectra, **(b)** first derivative of the normalized XANES, and **(c)** second derivative of the normalized XANES for Nb-containing materials (Nb K-edge). **(d)** EXAFS spectra (k^3-weighted) and fits for Nb-containing materials (Nb K-edge). Fitting parameters and fitting windows are included in Tables S1-S4.

Table S1. Fitting parameters of the Nb K-edge EXAFS spectrum of **Nb(O^{i}Pr)$_2$(OSi(O^{t}Bu)$_3$)$_3$.**

Scattering path	N	σ^2 / Å^2	R / Å
Nb-O	4	0.00294 ± 0.00046	1.910
Nb-O	1	0.00476 ± 0.00449	2.107
Nb-Si	1	0.01093 ± 0.00676	2.769
Nb-O-Si	2	0.00290 ± 0.00281	3.514
Nb-Si	2	0.00713 ± 0.00656	3.642

$3 < k < 14.1$, $S_0^2 = 1$, R-score = 0.01519, ΔE = -2.535 eV; $1 < R < 3.6$

The fitted spectrum of **Nb(O^{i}Pr)$_2$(OSi(O^{t}Bu)$_3$)$_3$** provides a good agreement with the presumed molecular structure, which was constructed in analogy to that for Ta(OEt)$_2$(OSi(O^{t}Bu)$_3$)$_3$[7] and subsequently geometrically optimized using force fields. This indicates that (i) amplitude reduction factor S_0^2 approaches 1 and that (ii) the molecule preserved its integrity during the XAS experiment.

Table S2. Fitting parameters of the Nb *K*-edge EXAFS spectrum of **Nb@SiO$_2$.**

Scattering path	N	σ^2 / Å^2	R / Å
Nb-O	2.1	0.00178 ± 0.00064	1.953
Nb-O	1.9	0.00840 ± 0.00423	2.152
Nb-Si	2.1	0.01897 ± 0.00911	2.821
Nb-O-Si	3.3	0.00926 ± 0.00861	3.598

3.2 < k < 13.8, S_0^2 = 1, R-score = 0.0049, ΔE = 7.44 eV; 1 < R < 3.1 Å

Table S3. Fitting parameters of the Nb *K*-edge EXAFS spectrum of **Cu/Nb@SiO$_2$.**

Scattering path	N	σ^2 / Å^2	R / Å
Nb-O	3.2	0.00759 ± 0.00135	1.949
Nb-O	2	0.00941 ± 0.00443	2.144
Nb-Si	0.9	0.00942 ± 0.00541	2.794
Nb-O-Si	2.7	0.01088 ± 0.00653	3.685

2.9 < k < 13.5; S_0^2 = 1, R-score = 0.06954, ΔE = 2.47 eV, 1 < R < 3.2

Table S4. Fitting parameters of the Nb *K*-edge EXAFS spectrum of **Cu/Nb@SiO$_2$ (spent).**

Scattering path	N	σ^2 / Å^2	R / Å
Nb-O	3.9	0.00985 ± 0.00095	1.919
Nb-Si	2.5	0.01658 ± 0.00474	2.782
Nb-O-Si	2.3	0.00377 ± 0.00360	3.325
Nb-O-Si	2.7	0.00563 ± 0.00181	3.503

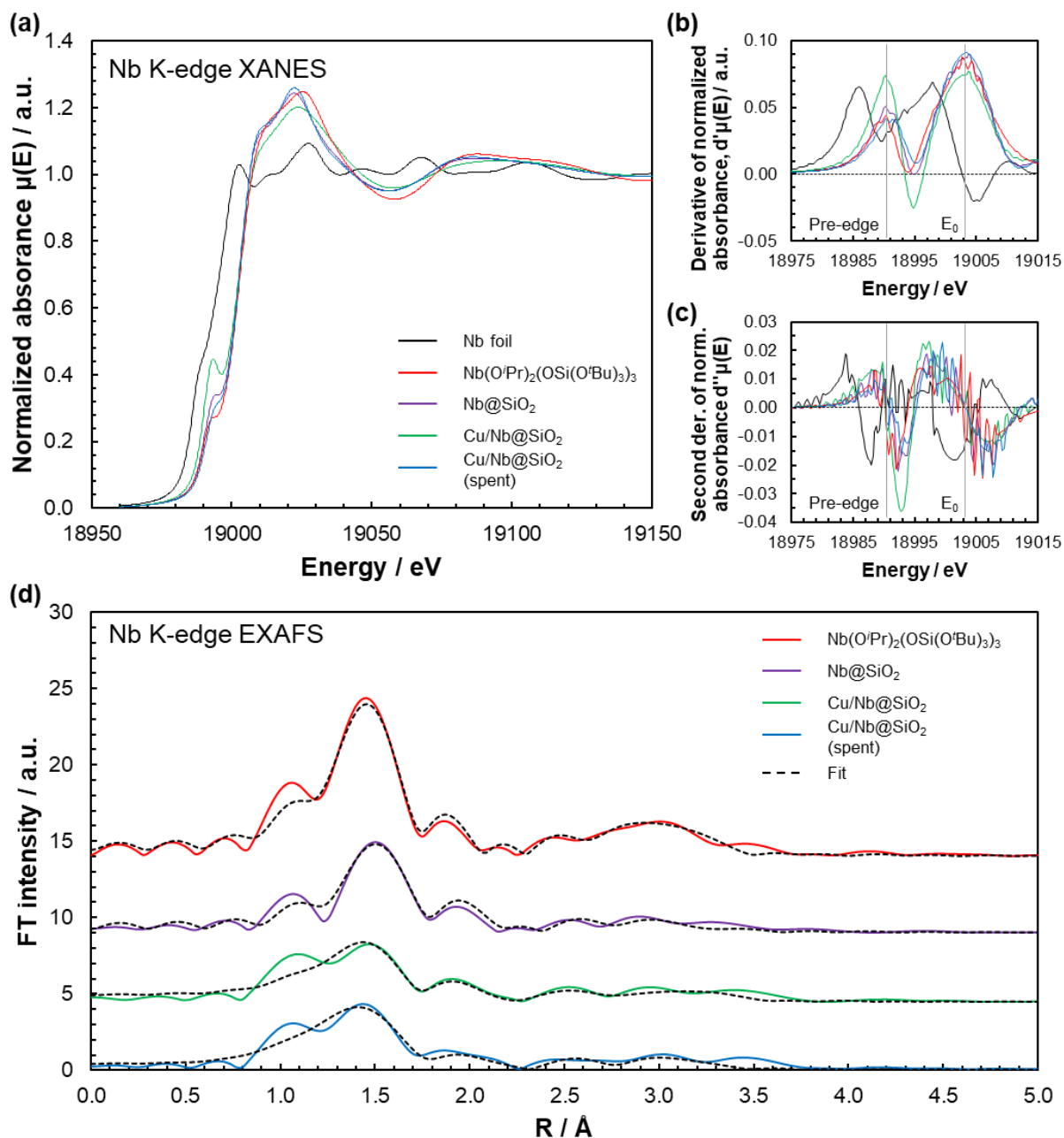2.8 < k < 13.8; S_0^2 = 1, R-score = 0.0447, ΔE = -9.85 eV, 1 < R < 3.2

Figure S5. (a) Normalized XANES spectra, **(b)** first derivative of the normalized XANES, and **(c)** second derivative of the normalized XANES for Ta-containing materials (Ta L_1-edge). **(d)** EXAFS spectra (k^3-weighted) and fits for Ta-containing materials (Ta L_3-edge). Fitting parameters and fitting windows are included in Tables S5-S8.

Table S5. Fitting parameters of the Ta L_3-edge EXAFS spectrum of **Ta(O^{i}Pr)$_2$(OSi(O^{t}Bu)$_3$)$_3$.**

Scattering path	N	σ^2 / Å^2	R / Å
Ta-O	5	0.00249 ± 0.00025	1.903
Ta-O	1	0.00476 ± 0.00340	2.296
Ta-O-Si	3.5	0.00163 ± 0.00127	3.504
Ta-Si	3	0.01252 ± 0.01241	3.729

2.8 < k < 12.8, S_0^2 = 1, R-score = 0.00620, ΔE = 8.08 eV, 1 < R < 3.3

The fitted spectrum of **Ta(O^{i}Pr)$_2$(OSi(O^{t}Bu)$_3$)$_3$** provides a good agreement with the presumed molecular structure, which was constructed in analogy to that for Ta(OEt)$_2$(OSi(O^{t}Bu)$_3$)$_3$[7] and subsequently geometrically optimized using force fields. This indicates that (i) amplitude reduction factor S_0^2 approaches 1 and that (ii) the molecule preserved its integrity during the XAS experiment.

Table S6. Fitting parameters of the Ta L_3-edge EXAFS spectrum of **Ta@SiO$_2$.**

Scattering path	N	σ^2 / Å^2	R / Å
Ta-O	3	0.00178 ± 0.00057	1.920
Ta-O	1.8	0.00681 ± 0.00260	1.810
Ta-Si	2	0.00780 ± 0.00268	3.212

$3 < k < 13.8$, $S_0^2 = 1$, R-score = 0.00999, $\Delta E = 6.722$ eV, $1 < R < 2.9$

Table S7. Fitting parameters of the Ta L_3-edge EXAFS spectrum of **Cu/Ta@SiO$_2$.**

Scattering path	N	σ^2 / Å^2	R / Å
Ta-O	4.5	0.00549 ± 0.00140	1.901
Ta-Si	2.6	0.00492 ± 0.00449	3.207

$2.6 < k < 9.5$, $S_0^2 = 1$, R-score = 0.06554, $\Delta E = 8.13$ eV, $1 < R < 3.3$

n.b.: The spectrum for Cu/Ta@SiO$_2$ had a relatively low edge jump, resulting in monochromator 'glitches' of large amplitude at $k > 9.5$. As a result, the fitting window was constrained to a smaller width for this spectrum, and only two scattering paths were fitted. Nevertheless, the spectrum is very similar to that for Cu/Ta@SiO$_2$ (spent), which was of sufficient quality for an extended fit, suggesting the absence of Ta agglomerates.

Table S8. Fitting parameters of the Ta L_3-edge EXAFS spectrum of **Cu/Ta@SiO$_2$ (spent).**

Scattering path	N	σ^2 / Å^2	R / Å
Ta-O	4.6	0.00523 ± 0.00044	1.914
Ta-Si	3	0.00824 ± 0.00214	3.264
Ta-O-Si	2.1	0.00505 ± 0.00467	3.804

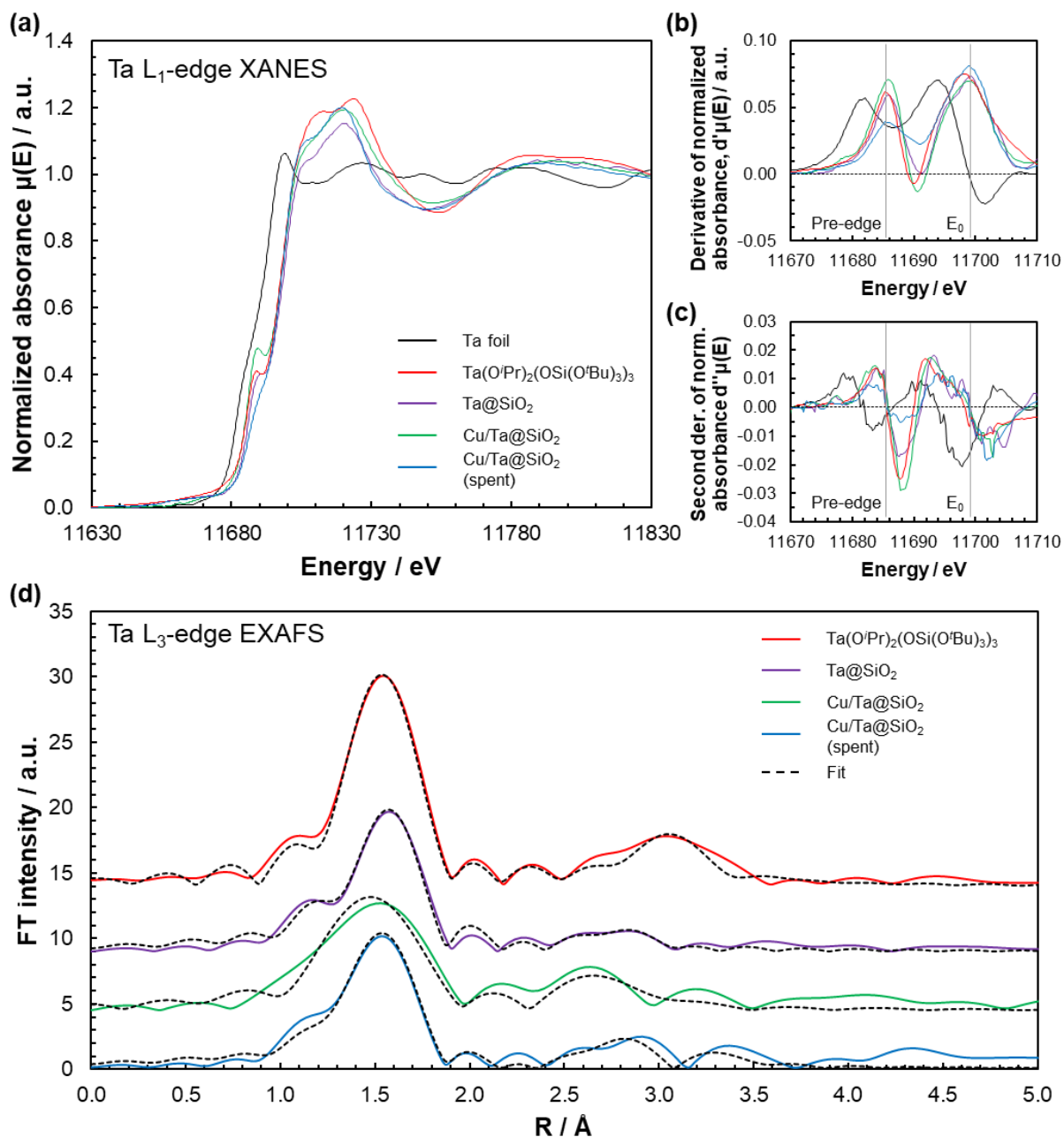$3 < k < 13.8$, $S_0^2 = 1$, R-score = 0.02498, $\Delta E = 8.06$ eV, $1 < R < 3.4$
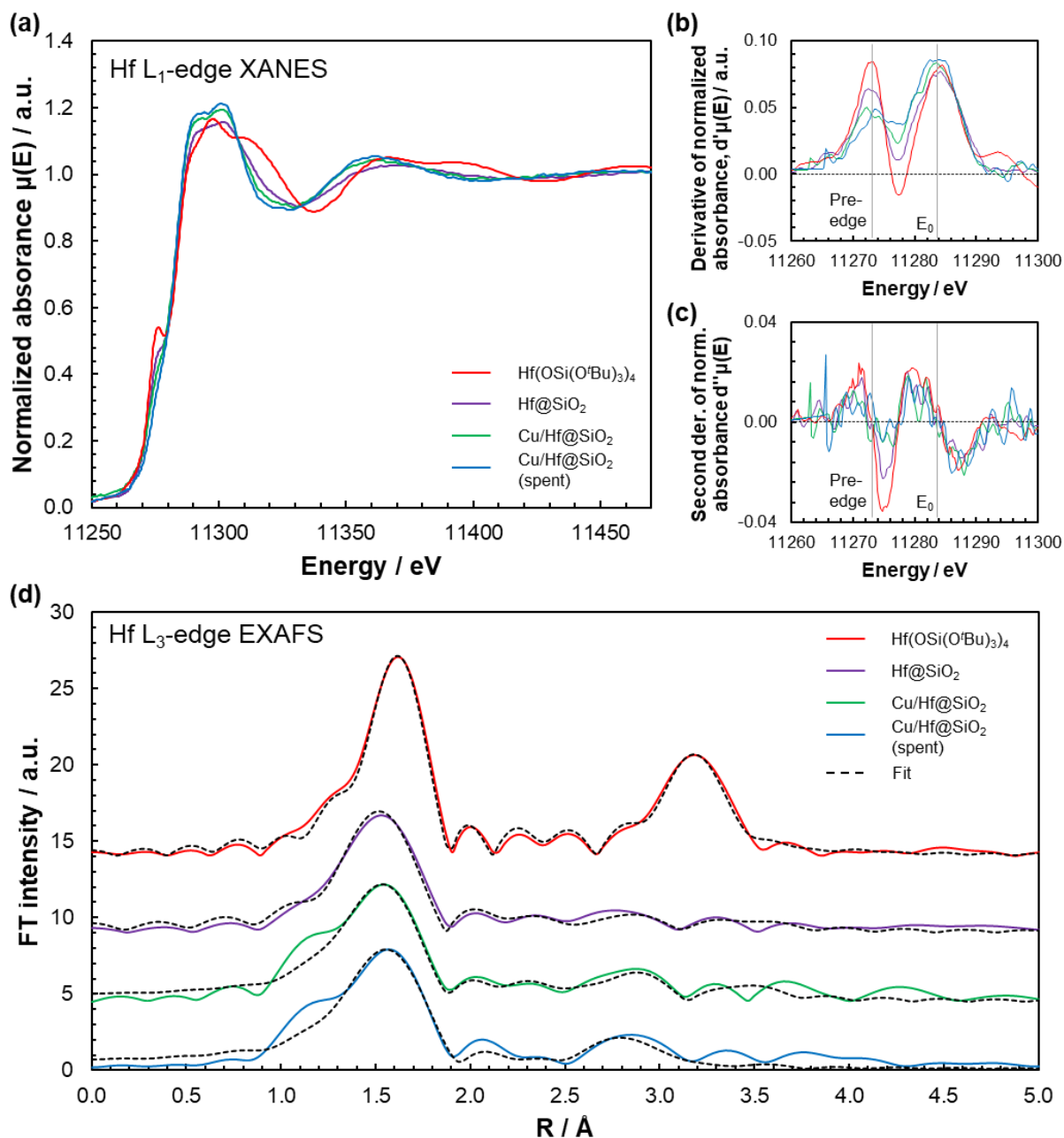
Figure S6. (a) Normalized XANES spectra, **(b)** first derivative of the normalized XANES, and **(c)** second derivative of the normalized XANES for Hf-containing materials (Hf L_1 -edge). **(d)** EXAFS spectra (k^3-weighted) and fits for Hf-containing materials (Hf L_3-edge). Fitting parameters and fitting windows are included in Tables S9-S12.

Table S9. Fitting parameters of the Hf L_3-edge EXAFS spectrum of **Hf(OSi(OᵗBu)₃)₄.**

Scattering path	N	σ^2 / Å²	R / Å
Hf-O	4	0.00289 ± 0.00020	1.955
Hf-O	0.5	0.00459 ± 0.00405	2.380
Hf-Si	0.5	0.00283 ± 0.00212	2.992
Hf-O-Si	3	0.00139 ± 0.00045	2.557
Hf-Si	3.5	0.01600 ± 0.00871	3.685

2.8 < k < 16, S_0^2 = 1, R-score = 0.00761, ΔE = 8.135 eV, 1 < R < 3.3

S16

The fitted spectrum of **Hf(OSi(O^{t}Bu)$_3$)$_4$** provides a good agreement with the crystallographic data,[3] which shows a 1:1 mixture of 4- and 5-coordinate Hf (the latter with one κ^2 OSi(O^{t}Bu)$_3$ ligand). This indicates that (i) the amplitude reduction factor S_0^2 approaches 1 and that (ii) the molecule preserves its integrity during the XAS experiment.

Table S10. Fitting parameters of the Hf L_3-edge EXAFS spectrum of **Hf@SiO$_2$.**

Scattering path	N	σ^2 / Å^2	R / Å
Hf-O	3.8	0.00491 ± 0.00051	1.932
Hf-Si	2.9	0.01489 ± 0.00407	2.940
Hf-O-Si	1.9	0.00432 ± 0.00349	3.547
Hf-O-Si	2.5	0.00508 ± 0.00488	3.732

2.8 < k < 12.6, S_0^2 = 1, R-score = 0.01751, ΔE = -0.342 eV, 1 < R < 3.2

Table S11. Fitting parameters of the Hf L_3-edge EXAFS spectrum of **Cu/Hf@SiO$_2$.**

Scattering path	N	σ^2 / Å^2	R / Å
Hf-O	5.4	0.00777 ± 0.00073	1.959
Hf-Si	2.2	0.00988 ± 0.00335	2.935
Hf-O-Si	2.4	0.00360 ± 0.00307	3.738
Hf-O-Si	2.0	0.00303 ± 0.00238	3.565

2.7 < k < 13.3, S_0^2 = 1, R-score = 0.03371, ΔE = -2.080 eV, 1 < R < 3.4

Table S12. Fitting parameters of the Hf L_3-edge EXAFS spectrum of **Cu/Hf@SiO$_2$ (spent).**

Scattering path	N	σ^2 / Å^2	R / Å
Hf-O	6	0.00818 ± 0.00093	1.984
Hf-Si	2	0.01095 ± 0.00684	2.979
Hf-Si	1.6	0.00630 ± 0.00573	3.295
Hf-O-Si	3.8	0.01390 ± 0.00942	3.704

2.7 < k < 12.7, S_0^2 = 1, R-score = 0.03982, ΔE = 0.031 eV, 1 < R < 3.3

Section S4: Infrared spectra for catalysts with adsorbed CO
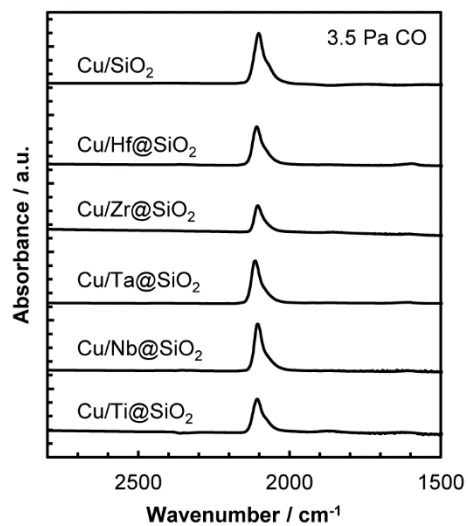
Figure S7. Difference IR spectra for Cu/SiO$_2$ and Cu/M@SiO$_2$ (M = Ti, Zr, Hf, Nb, or Ta) with adsorbed CO (3.5 Pa CO, 298 K), compared to samples under vacuum. Absorbance features for ν(C-O) of atop-bound CO completely disappeared after vacuum treatment following adsorption of CO, which is consistent with the reversible adsorption of CO on Cu.

Section S5: Scheme of site requirements for CO_2 hydrogenation pathways
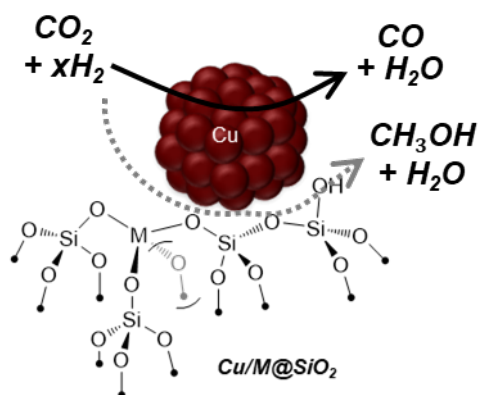
Scheme S1. Schematic representation of CO_2 hydrogenation pathways on Cu/M@SiO$_2$. CO and CH$_3$OH are formed in parallel reactions. CO is formed on the same site as Cu/SiO$_2$ (likely a Cu nanoparticle, indicated by the black arrow), while CH$_3$OH is formed on a Cu-M interfacial site (indicated by the grey dashed arrow).

Section S7: CH₃OH and CO formation rates for Cu/M@SiO₂ and Cu/SiO₂ catalysts
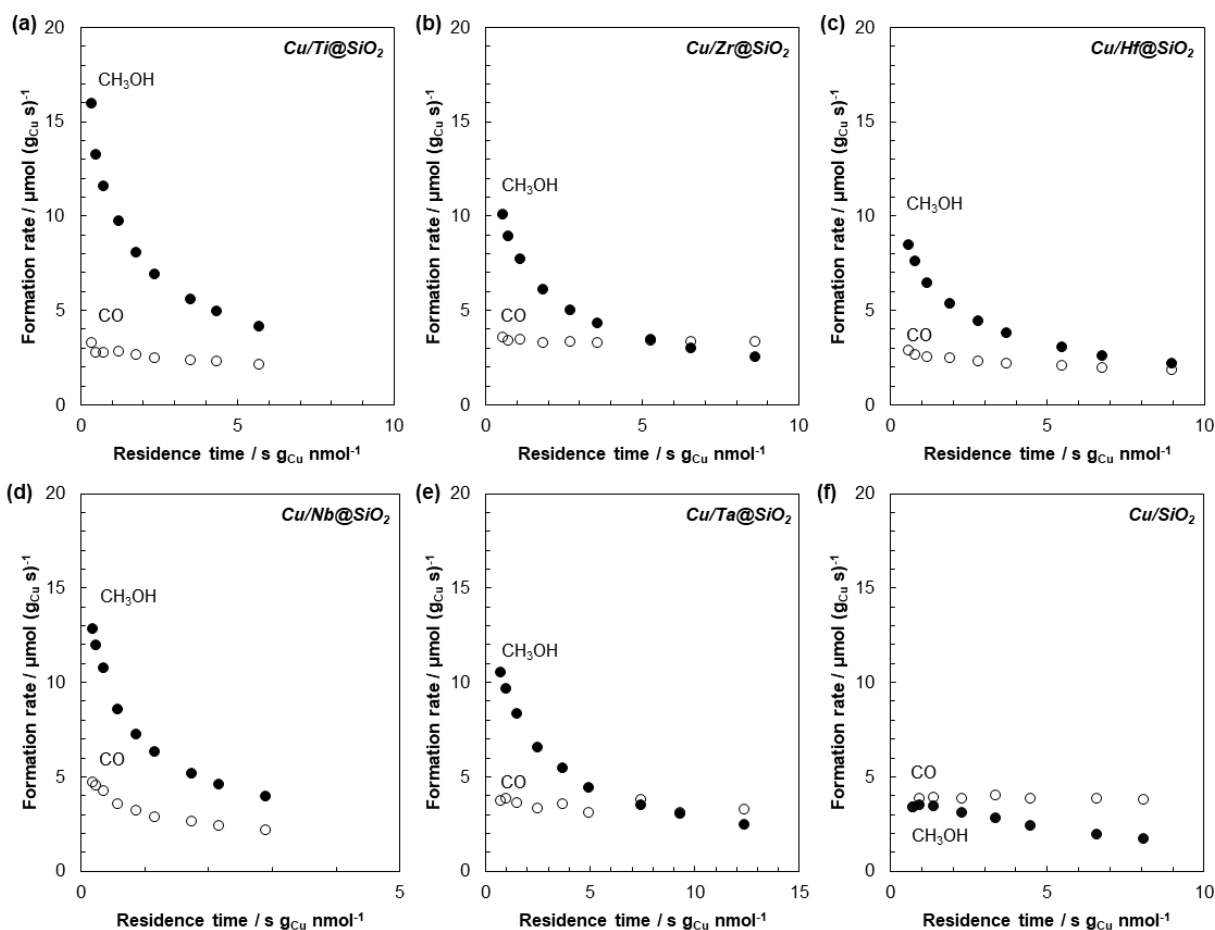
Figure S8. CH₃OH (filled) and CO (unfilled) formation rates as a function of residence time for **(a)** Cu/Ti@SiO₂, **(b)** Cu/Zr@SiO₂, **(c)** Cu/Hf@SiO₂, **(d)** Cu/Nb@SiO₂, **(e)** Cu/Ta@SiO₂, and **(f)** Cu/SiO₂.

Table S13. Reaction rates on M@SiO₂ and physical mixtures of Cu/SiO₂+M@SiO₂ (1:1 mass).

Catalyst	Initial CH₃OH formation rate / μmol $(g_{Cu}$ s$)^{-1}$ [a]	Initial CO formation rate / μmol $(g_{Cu}$ s$)^{-1}$ [b]
Ti@SiO₂	-- [c]	-- [c]
Nb@SiO₂	-- [c]	-- [c]
Ta@SiO₂	-- [c]	-- [c]
Zr@SiO₂	-- [c]	-- [c]
Hf@SiO₂	-- [c]	-- [c]
Cu/SiO₂+ Ti@SiO₂	3.65 ± 0.12	3.80 ± 0.02
Cu/SiO₂+ Nb@SiO₂	3.59 ± 0.17	3.67 ± 0.13
Cu/SiO₂+ Ta@SiO₂	3.63 ± 0.13	3.80 ± 0.05
Cu/SiO₂+ Zr@SiO₂	3.57 ± 0.10	3.78 ± 0.07
Cu/SiO₂+ Hf@SiO₂	3.54 ± 0.15	3.70 ± 0.10

[a] error represents 95% confidence interval. [b] error represents standard error. [c] below detection limits of instrument.

Section S8: Infrared spectra of catalysts with adsorbed pyridine, isobars, and pyridine adsorption enthalpies

For Cu/M@SiO$_2$ materials (M = Ti, Zr, Hf), two additional bands are seen compared to the spectra for their respective M@SiO$_2$ materials (1600 cm^{-1}, 1480 cm^{-1}), similar to those observed for Cu/SiO$_2$. Subtracting the pyridine adsorption band at 1444 cm^{-1} for Cu/SiO$_2$ from the spectra of Cu/M@SiO$_2$ materials, assuming this band arises from adsorption on the Cu metal, yields areas and FWHM of the remaining bands that are nearly the same as for the respective M@SiO$_2$ materials (Table S14). For Ta and Nb materials, the Cu/SiO$_2$ adsorption bands are not observed; nevertheless, the areas and FWHM of the band at 1450 cm^{-1} are similar despite the presence of Cu (Table S14). These data together indicate that M@SiO$_2$ sites are essentially identical to those after Cu nanoparticles have been dispersed on the support. Thus, the pyridine band areas measured for M@SiO$_2$, and therefore for Cu/M@SiO$_2$, are the appropriate quantity to measure.
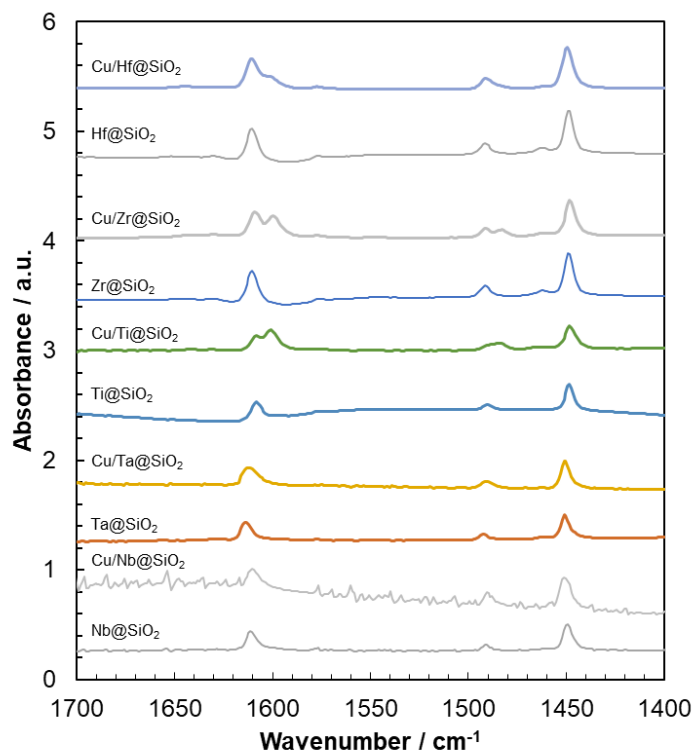
Figure S9. Difference IR spectra for materials with pyridine adsorbed then desorbed at 373 K and spectra prior to absorption, normalized by the area of the Si-O-Si overtone bands, for M@SiO$_2$ and Cu/M@SiO$_2$ materials.

Table S14. Band area and FWHM for the pyridine vibrational band at 1450 cm^{-1}.

	Cu/Ti@SiO$_2$	Cu/Zr@SiO$_2$	Cu/Hf@SiO$_2$	Cu/Nb@SiO$_2$	Cu/Ta@SiO$_2$
Band area	2.1	1.5	3.0	3.0	3.7
FWHM	5.7	5.8	5.8	5.7	5.8
	Ti@SiO$_2$	Zr@SiO$_2$	Hf@SiO$_2$	Nb@SiO$_2$	Ta@SiO$_2$
Band area	2.0	1.6	2.8	2.9	3.8
FWHM	5.7	5.8	5.8	5.8	5.8

(a)

(b)
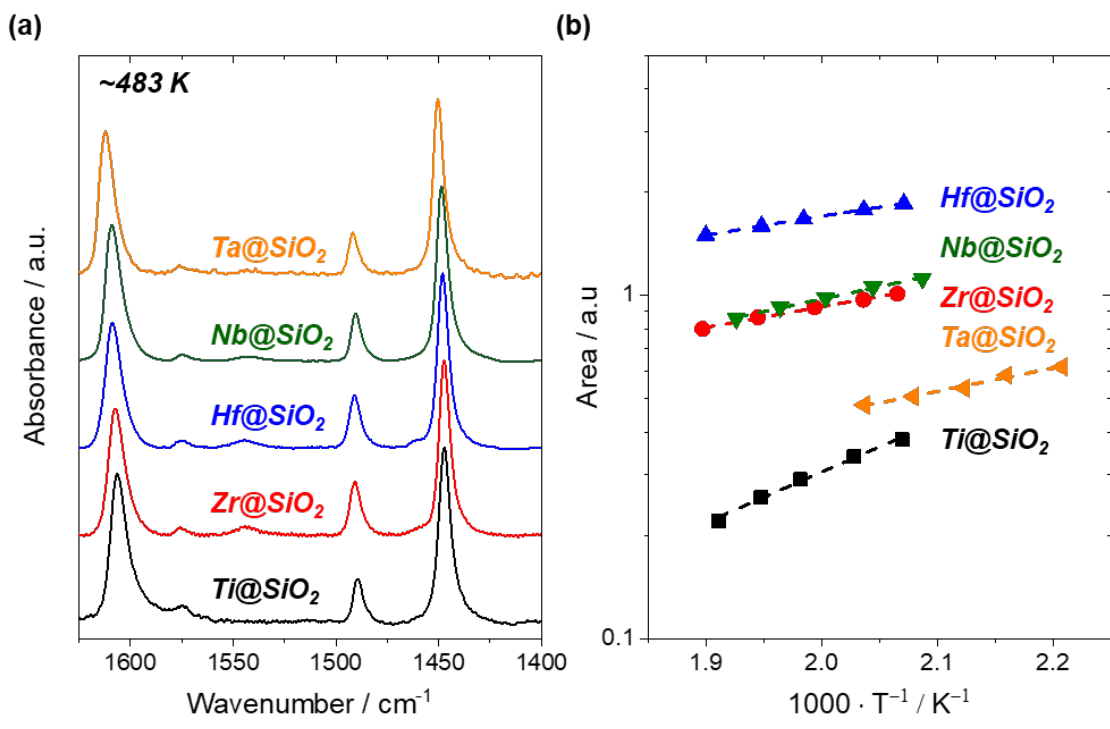
Figure S10. (a) Normalized IR spectra of M@SiO$_2$ (treated by flowing He for 2 h at 573 K) with adsorbed pyridine (483 K, 0.1 kPa pyridine). **(b)** Isobars (0.1 kPa pyridine) for M@SiO$_2$ (453-523 K), using the areas of the pyridine bands at 1450 cm^{-1}. Dashed lines show the fit of the van't Hoff equation.

Table S15. Pyridine adsorption enthalpies for M@SiO$_2$, determined from isobars (0.1 kPa pyridine; 483-523 K). Errors represent standard error.

Material	$\Delta H_{ads,pyridine}$ / kJ mol^{-1}
Ti@SiO$_2$	-29 ± 1
Nb@SiO$_2$	-15 ± 1
Ta@SiO$_2$	-13 ± 1
Zr@SiO$_2$	-12 ± 1
Hf@SiO$_2$	-10 ± 1

Section S9: DFT Calculation of ^{13}C NMR Chemical Shifts, Comparison with Measured Values, and Natural Chemical Shielding Analysis

Computational Details

Geometry optimizations and vibrational analysis were performed with the B3LYP[13] functional in combination with a 6-311G(d)[14,15] basis set (for C, H, Si and O) and the Stuttgart-Dresden effective core potential (SDD)[16,17] (for Ti, Zr, Hf, Nb, Ta) and the associated basis set using Gaussian09 (revision D.01).[18] NMR calculations on metal complexes were performed at the same level of theory with the Gauge-Independent Atomic Orbital (GIAO)[19,20] method and an ultrafine integration grid. The ^{13}C chemical shift was referenced to tetramethylsilane (TMS; set to 0 ppm) from the calculated chemical shielding according to:

$$\delta_{iso} = \delta_{TMS} - \delta_{iso} \qquad\qquad\qquad\qquad\qquad \text{(Eq. 1)}$$

where δ_{iso} is the isotropic ^{13}C chemical shift, δ_{TMS} is the chemical shielding of TMS (0 ppm), and δ_{iso} is the calculated ^{13}C chemical shielding.

Natural chemical shielding (NCS) analysis of the optimized cluster models was performed with ADF 2014[21,22] with the Gauge-Independent Atomic Orbital (GIAO) method and a full electron TZP[23] basis set and revPBE functional.[24] Relativistic effects were included by the two component zero order regular approximation (ZORA) approach including spin-orbit coupling.[25] The NMR chemical shielding tensors components were deconvoluted into the contributions of the individual natural localized molecular orbitals (NLMO)[26,27] obtained by the NBO 6.0 program[28] in its scalar-relativistic framework. Chemical shift tensors were plotted using a Mathematica script provided by Autschbach and coworkers.[29,30]

[13]C Chemical Shift Calculations

In order to understand the measured ^{13}C chemical shifts of methoxy species in ssNMR, two series of methoxy species were optimized and their respective chemical shifts were calculated using DFT methods: (1) molecular models of methoxy complexes, and (2) methoxy coordinated to cluster models of SiO_2 with a metal site, coordinated by three (Ti, Zr, Hf) or four (Nb, Ta) siloxy ligands and one methoxy ligand; these SiO_2-based cluster models are used for NCS analysis in the following section. The results are summarized in Table S16. CH_3OH shows a chemical shift at δ_{iso} = 54 ppm and is close to the experimentally measured value (δ_{iso} = 49 ppm, measured in C_6D_6[31]). The calculated chemical shift for CH_3OH is similar to that for $Si(OCH_3)_4$ (δ_{iso} = 53 ppm), indicating that measured signals at similar chemical shifts could be interpreted as either species. Measured chemical shifts for $[Nb(OCH_3)_5]_2$ (δ_{iso} = 61.1 and 60.5 ppm, measured in C_6D_6; Figure S26), $[Ta(OCH_3)_5]_2$ (δ_{iso} = 59.6 ppm, measured in C_6D_6; Figure S30), and $[Ti(OCH_3)_4]_2$ (61 and 77 ppm; Figure S31) are similar to their calculated molecular models (δ_{iso} = 61-68 ppm, 60-65 ppm, and 65-69 ppm, respectively).

For comparison with molecular models, the chemical shift of methoxy complexes of Ti, Zr, Hf, Nb and Ta as dimers were calculated. $[Ti(OCH_3)_4]$ has a ^{13}C chemical shift of δ_{iso} = 67 ppm while the dimer $[Ti(OCH_3)_4]_2$ has ^{13}C chemical shifts ranging between δ_{iso} = 65-69 ppm. Thus, they are similar to the experimentally measured ^{13}C chemical shift of $Ti(OCH_3)_4$ of δ_{iso} = 65 ppm (measured in C_6D_6). The calculated ^{13}C chemical shift of CH_3OH coordinated to $[Ti(OCH_3)_4]$ is δ_{iso} = 54 ppm, similar to free CH_3OH. This shows that the experimentally measured ^{13}C chemical shift in ssNMR of $Cu/Ti@SiO_2$ treated with [13]CO_2/H_2 corresponds to methoxy (OCH_3) (for the more downfield signal at 66 ppm) and CH_3OH coordinated to Ti(IV) surface sites at 49 ppm.

In case of $[Zr(OCH_3)_4]_2$ (δ_{iso} = 61-63 ppm), the ^{13}C chemical shift is less downfield than for $[Ti(OCH_3)_4]_{x = 1\ or\ 2}$ (δ_{iso} = 65-69 ppm). The corresponding ^{13}C chemical shift in ssNMR of $Cu/Zr@SiO_2$ treated with [13]CO_2/H_2 shows a major signal at 49 ppm but also shows a downfield shoulder (Figure 3 of the main text; Figure S11). Deconvolution of this feature (Figure S11) shows that the shoulder is located at 53 ppm and likely represents the $Zr-OCH_3$ intermediates (or strongly coordinated CH_3OH species), while the feature at 49 ppm is CH_3OH coordinated to Zr(IV) surface sites. The ^{13}C chemical shift for $[Hf(OCH_3)_4]_2$ (δ_{iso} = 59-61 ppm) is less downfield-shifted compared to $[Zr(OCH_3)_4]_2$ (δ_{iso} = 61-63 ppm) and more similar to that for CH_3OH (54 ppm). $Cu/Hf@SiO_2$ treated with [13]CO_2/H_2 shows only one major signal at around 49 ppm, and it is therefore indistinguishable whether this signal corresponds to CH_3OH or OCH_3 coordinated (or $Si(OCH_3)_4$).

For $[Nb(OCH_3)_5]_2$ the ^{13}C chemical shift ranges between δ_{iso} = 61-68 ppm. The signal observed in ssNMR at 62 ppm for $Cu/Nb@SiO_2$ treated with $^{13}CO_2/H_2$ likely corresponds to $Nb-OCH_3$ intermediates along with a less downfield shifted signal at 49 ppm likely corresponding to CH_3OH coordinated to Nb surface sites. The shoulder observed between the two main signals likely corresponds to more strongly coordinated CH_3OH species on Nb(V). Similarly, for $[Ta(OCH_3)_5]_2$ the ^{13}C chemical shift is between δ_{iso} = 60-65 ppm. The signal observed in ssNMR at 59 ppm for $Cu/Ta@SiO_2$ treated with $^{13}CO_2/H_2$ likely corresponds to $Ta-OCH_3$ intermediates along, with a less downfield signal at 49 ppm likely corresponding to CH_3OH coordinated to Ta surface sites. The shoulder observed between the two main signals likely corresponds to more strongly coordinated CH_3OH species on Ta(V).

The comparison between measured ($\delta_{iso,exp}$) and the mean of calculated ($<\delta_{iso,calc}>$) chemical shifts is shown in Figure S12.

Table S16. Calculated ^{13}C chemical shifts.

Compound	^{13}C chemical shift / ppm
CH_3OH	54
$[Si(OCH_3)_4]$	53
$[Ti(OCH_3)_4]$	67
$[Ti(OCH_3)_4(CH_3OH)]$	54 (CH_3OH); 65-69 (OCH_3)
$[Ti(OCH_3)_4]_2$	65-69
$CH_3O-Ti@SiO_2$	71
$[Zr(OCH_3)_4]_2$	61-63
$CH_3O-Zr@SiO$	66
$[Hf(OCH_3)_4]_2$	59-61
$CH_3O-Hf@SiO_2$	66
$[Nb(OCH_3)_5]_2$	61-68
$CH_3O-Nb@SiO_2$	69
$[Ta(OCH_3)_5]_2$	60-65
$CH_3O-Ta@SiO_2$	66

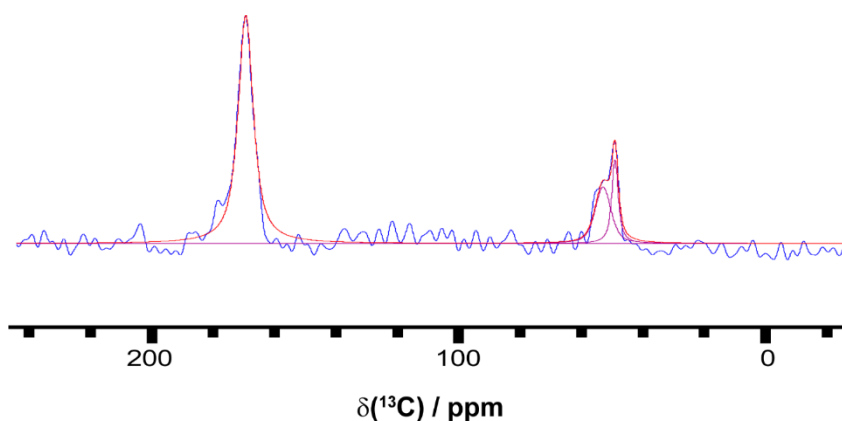**Figure S11.** Measured (blue) and deconvoluted (pink) ^{13}C ssNMR spectra for $Cu/Zr@SiO_2$, treated with $^{13}CO_2/H_2$.
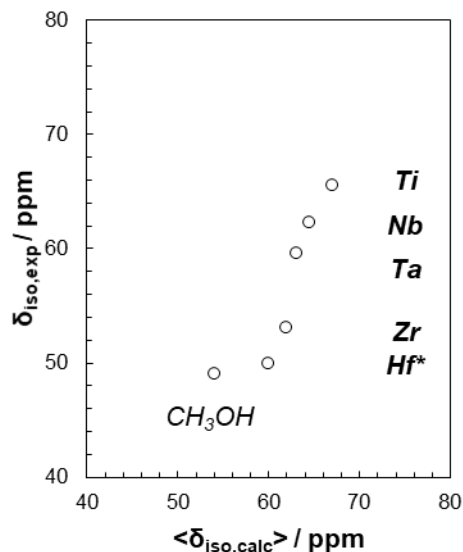
Figure S12. Mean of calculated ($<\delta_{iso,calc}>$) and measured ($\delta_{iso,exp}$) ^{13}C chemical shifts of molecular models for Ti-OCH$_3$, Zr-OCH$_3$, Hf-OCH$_3$*, Nb-OCH$_3$, Ta-OCH$_3$, and CH$_3$OH.
*For Hf-OCH$_3$, the chemical shift for the sole measured signal in the CH$_3$OH/OCH$_3$ region (48-66 ppm) was assumed to be the $\delta_{iso,exp}$ value for Hf-OCH$_3$ and not coordinated CH$_3$OH. The measured signal could also arise from OCH$_3$ coordinated to the Si of the support or from adsorbed CH$_3$OH.

Natural Chemical Shielding Analysis

The CH$_3$OH formation rates among the catalysts with Lewis acidic Ti, Zr, Hf, Nb, and Ta surface sites in Cu/M@SiO$_2$ (M = Ti, Zr, Hf, Nb, Ta) show the following trend: Ti > Nb > Ta > Zr > Hf. The same trend is observed for the measured ^{13}C chemical shift of the methoxy intermediate coordinated to Ti, Zr, Hf, Nb, and Ta; this correlation between the CH$_3$OH formation rate and the ^{13}C chemical shift of methoxy suggests the presence of a common underlying phenomenon. The ^{13}C chemical shift can be directly related to the electronic structure around the nucleus,[32] thus allowing the development of a relationship between the obtained catalytic results and the electronic properties (i.e., Lewis acidity induced by Ti, Zr, Hf, Nb, and Ta surface sites in Cu/M@SiO$_2$).

To model the methoxy ligand coordinated to the Lewis acidic surface sites (Ti, Zr, Hf, Nb, and Ta), cluster models of SiO$_2$ with a metal site (Ti, Zr, Hf, Nb, and Ta) coordinated by three (Ti, Zr, Hf) or four (Nb, Ta) siloxy ligands, and one methoxy ligand were constructed (Figure S13). The calculated ^{13}C chemical shifts (δ_{iso}) are in agreement and follow similar trends as with the experimentally measured ^{13}C chemical shift of methoxy in the CP-MAS NMR, albeit with chemical shift values that are similar among the three least deshielded metals (Ta, Zr and Hf) (Figure S13). The ^{13}C chemical shift (δ_{iso}) is further deconvoluted to obtain a clearer understanding of its relationship with the electronic structure surrounding the methoxy carbon.

CH₃O-Ti@SiO₂
δ_{iso}: 71 ppm

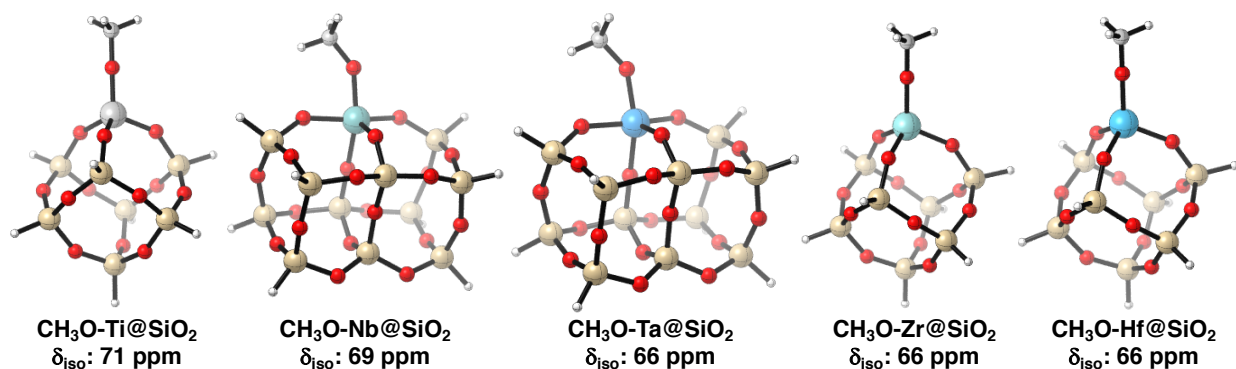**CH₃O-Nb@SiO₂**
δ_{iso}: 69 ppm

CH₃O-Ta@SiO₂
δ_{iso}: 66 ppm

CH₃O-Zr@SiO₂
δ_{iso}: 66 ppm

CH₃O-Hf@SiO₂
δ_{iso}: 66 ppm

Figure S13. Cluster models of M@SiO₂ (M = Ti, Zr, Hf, Nb, Ta) with a methoxy ligand coordinated to the metal (M) site and the isotropic chemical shift δ_{iso} of the carbon of methoxy obtained by scalar relativistic DFT calculations.

The isotropic ¹³C chemical shift (δ_{iso}) is the average of the three principal components of the chemical shift tensor:

$$\delta_{iso} = (\delta_{11} + \delta_{22} + \delta_{33})/3 \qquad \text{(Eq. 2)}$$

where individual components are denoted by δ_{ii} (i = 1, 2, or 3). The values of δ_{ii} can be obtained from the chemical shielding tensor principal components σ_{ii} by DFT calculations, with $\delta_{ii} \approx \sigma_{iso,ref} - \sigma_{ii}$. The chemical shielding tensor (σ_{iso}) can be further split into diamagnetic (σ_{dia}) and paramagnetic (σ_{para}) contributions: $\sigma_{iso} = \sigma_{dia} + \sigma_{para}$. The former arises from the core orbitals and is rather insensitive to changes in the electronic environment around the nucleus. In contrast, the latter is sensitive to the frontier orbitals (i.e., the orbitals close to the HOMO-LUMO gap) and therefore the changes in the electronic environment around the nucleus. More precisely, the paramagnetic contribution arises from magnetically induced admixture of the ground state with the excited states via the angular momentum operator ($\hat{L}_i$) that acts in the direction of σ_{ii}. The effect of the angular momentum operator can be understood conceptually by the orbital-rotation model: deshielding (the decrease in chemical shielding value/increase in chemical shift value) of the chemical shielding tensor principal components (σ_{ii}) occurs when an occupied orbital can be superimposed with a virtual orbital via rotation of 90° along the direction of the angular momentum operator (Figure S14a).[33] The deshielding is greater if the difference in energy between the occupied and virtual orbital is small, hence its effect is more pronounced for frontier orbitals.[33] The link between the chemical shielding and frontier orbitals can be made by natural chemical shielding (NCS) analysis that allows deconvolution of the chemical shielding to contributions of the natural localized molecular orbitals (NLMO).[27]
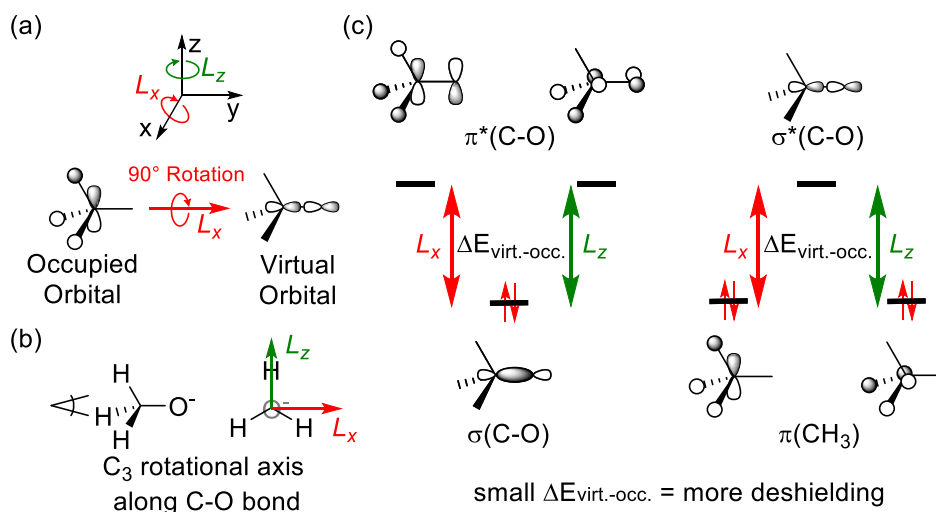
Figure S14. (a) Orientation of the angular momentum operators $\hat{L}_x$ and $\hat{L}_z$. **(b)** Visualization of the C₃ rotational axis with respect to the angular momentum operators $\hat{L}_x$ and $\hat{L}_z$. **(c)** Molecular orbitals mainly responsible for deshielding in case of CH₃O⁻. (Left) Coupling between the occupied σ(C-O) and the virtual π*(C-O) orbitals via $\hat{L}_x$ and $\hat{L}_z$. (Right) Coupling between the occupied π(CH₃) and the virtual σ*(C-O) orbitals via $\hat{L}_x$ and $\hat{L}_z$.

The principal components of the chemical shielding tensor have a similar orientation for all the cluster models (Figure S15). σ_{11} and σ_{22} are both directed perpendicular to the C-O bond (Figure S14a and S15) with σ_{11} being directed along the x-direction and σ_{22} along the z-direction, and corresponds to the angular momentum operator $\hat{L}_x$ and $\hat{L}_z$, respectively. σ_{33} is oriented along the C-O bond in the y-direction corresponding to $\hat{L}_y$ (Figure S15). The difference in the isotropic chemical shielding among the cluster models is mainly a result of the paramagnetic contribution of the two principal components σ_{11} and σ_{22} (Figure S17-19).
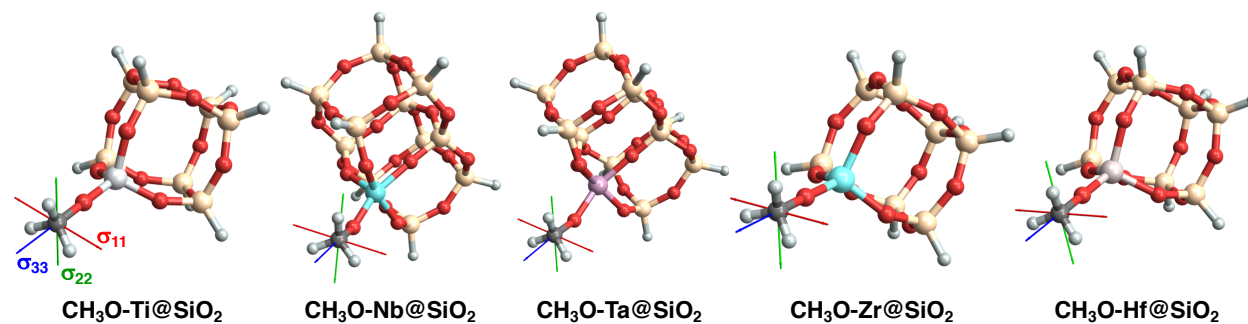
Figure S15. Chemical shielding tensor orientation (σ_{11}: red, σ_{22}: green, σ_{33}: blue) for the M-OCH$_3$ cluster carbon.

Further analysis of the contribution of each individual NLMO of $\sigma_{11\text{-para}}$ (Figure S20) and $\sigma_{22\text{-para}}$ (Figure S21) shows that the main contribution originates from the σ(C-O) orbital and remains constant among the different metals. The second largest contribution arises from the C-H bonding NLMO and corresponds to the π(CH$_3$) molecular orbitals. These values become less negative in the order: Ti, Nb, Ta, Zr, and Hf, similar to trends observed for CH$_3$OH formation rates. It should be noted that $\hat{L}_x$ and $\hat{L}_z$, are complementary to each other and couple similar types of orbitals due to the C$_3$ rotational axis of the methoxy ligand (Figure S14b and S16). The large contribution from the σ(C-O) orbital is the result of the coupling with the π^*(C-O) orbital, which is perpendicular both to the direction of the $\hat{L}_x$ and $\hat{L}_z$ operators (Figure S14c, S22, and S23). The π(CH$_3$) orbitals are coupled with the σ^*(C-O) orbital through $\hat{L}_x$ and $\hat{L}_z$ (Figure S14c). The decreased (less negative) contribution correlates with the binding strength of the OCH$_3$ on M (in the order: M = Ti, Nb, Ta, Zr, Hf). A stronger M-O bond weakens the C-O bond and leads to a decrease in the σ^*(C-O) orbital energy and thus a smaller energy gap and more deshielding (Figure S22 and S23). NCS analysis therefore reveals that the change in ^{13}C chemical shift of a methoxy ligand coordinated to different metal sites is directly related to the binding strength (i.e., the Lewis acid strength of the metal) and affects the ^{13}C chemical shift, leading to a more downfield chemical shift with increasing Lewis acid strength.
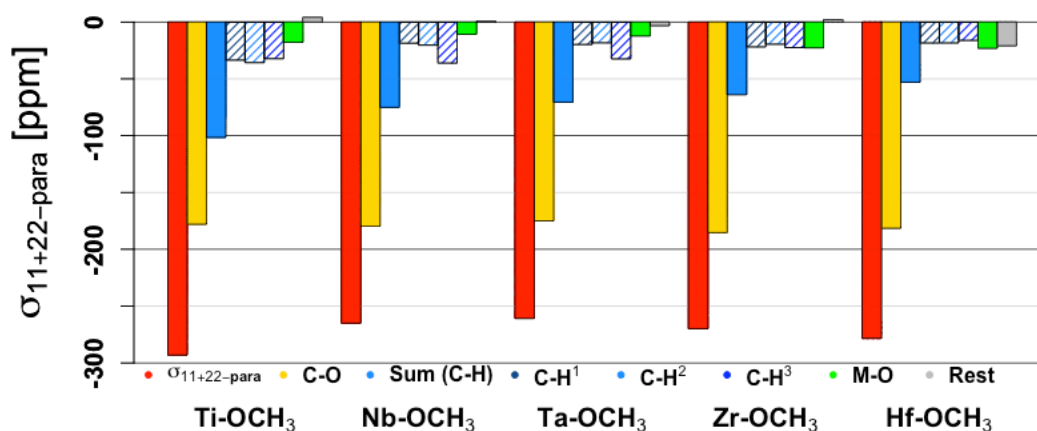
Figure S16. Sum of the paramagnetic chemical shielding contribution of $\sigma_{11\text{-para}}$ and $\sigma_{22\text{-para}}$ for the methoxy carbon of the cluster models split into the individual NLMO contributions.
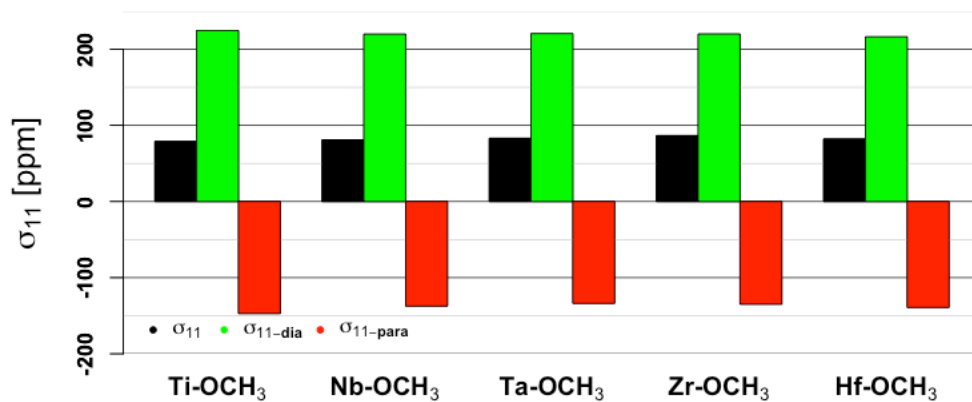
Figure S17. Chemical shielding contribution of σ_{11} for the methoxy carbon of the cluster models split in the diamagnetic ($\sigma_{11\text{-dia}}$) and paramagnetic ($\sigma_{11\text{-para}}$) contribution.
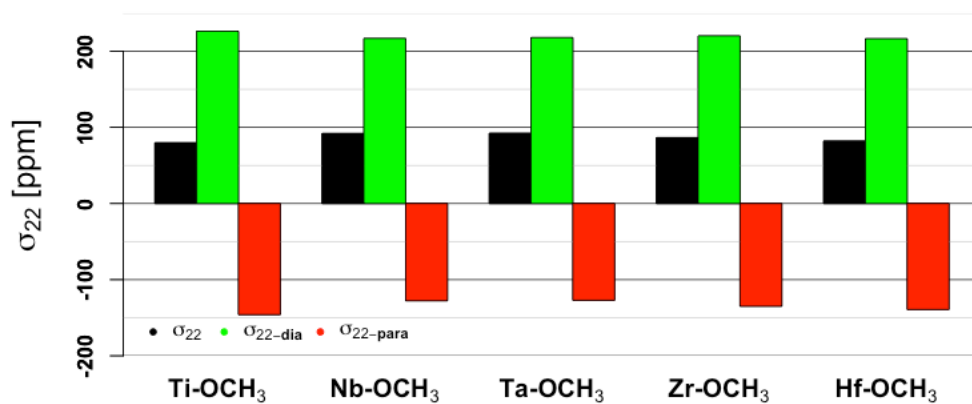
Figure S18. Chemical shielding contribution of σ_{22} for the methoxy carbon of the cluster models split in the diamagnetic ($\sigma_{22\text{-dia}}$) and paramagnetic ($\sigma_{22\text{-para}}$) contribution
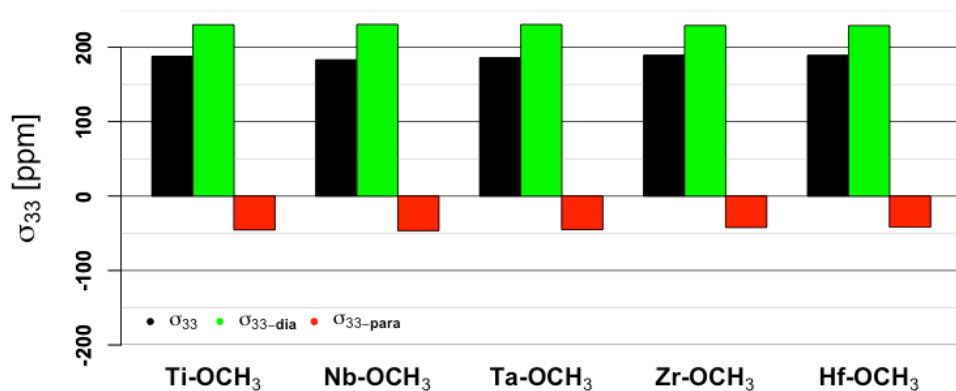
Figure S19. Chemical shielding contribution of σ_{33} for the methoxy carbon of the cluster models split in the diamagnetic ($\sigma_{33\text{-dia}}$) and paramagnetic ($\sigma_{33\text{-para}}$) contribution
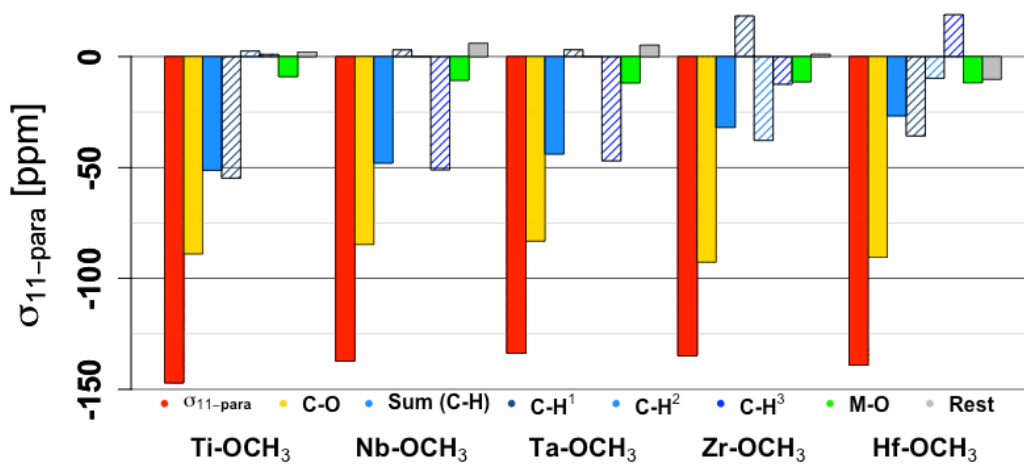
Figure S20. Paramagnetic chemical shielding contribution of $\sigma_{11\text{-para}}$ for the methoxy carbon of the cluster models split into the individual NLMO contributions.
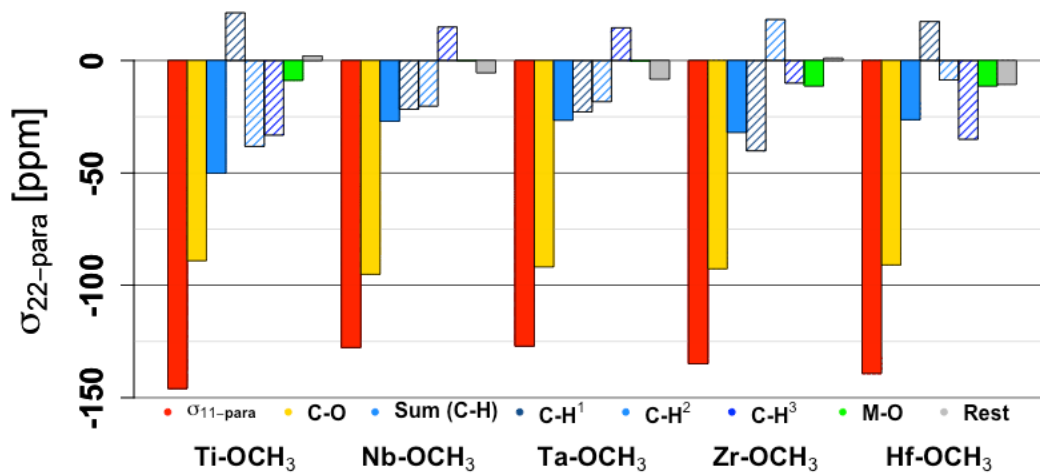
Figure S21. Paramagnetic chemical shielding contribution of $\sigma_{22\text{-para}}$ for the methoxy carbon of the cluster models split into the individual NLMO contributions.
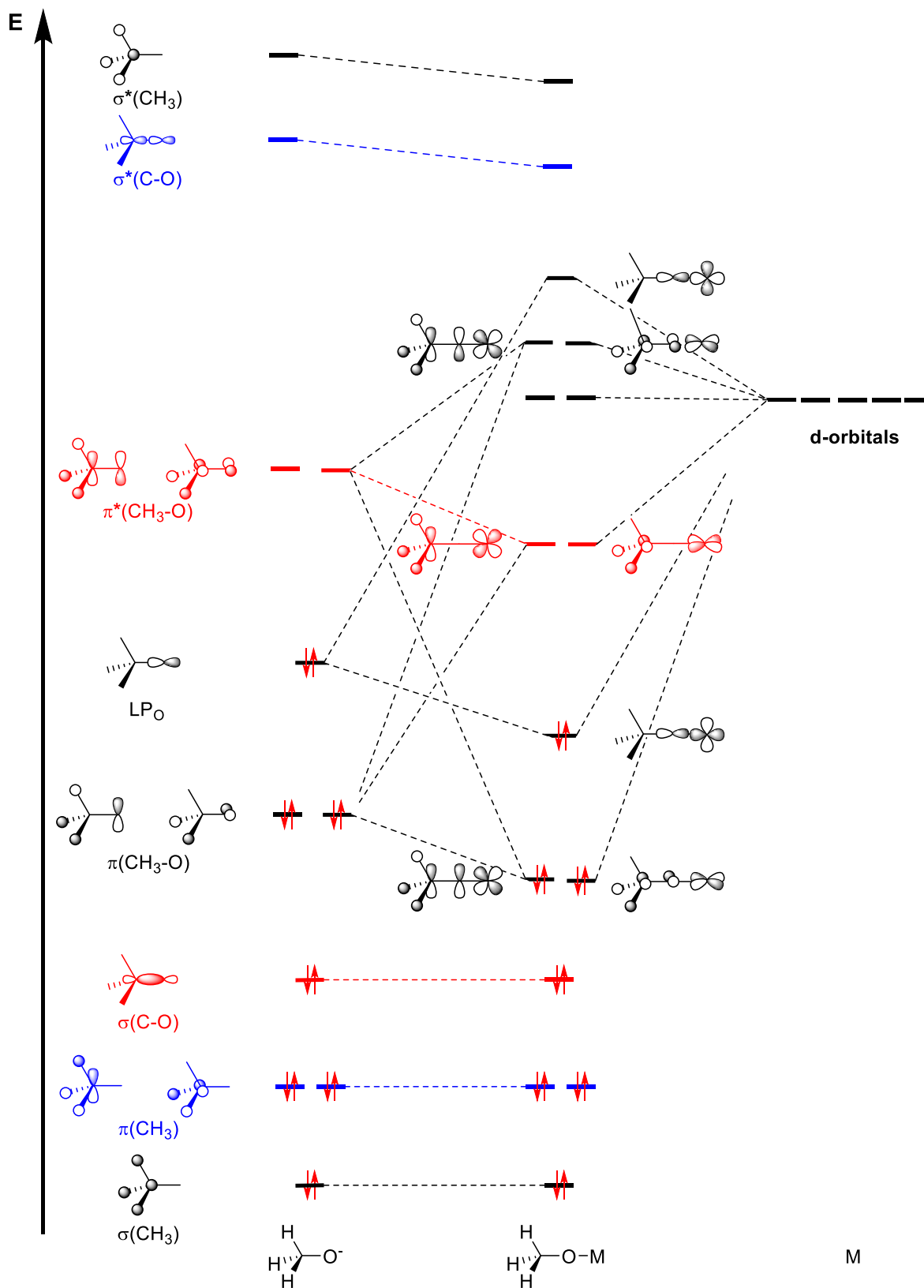
Figure S22. MO scheme of the σ and π interaction between the methoxy ligand and d⁰ metal. The orbitals responsible for the deshielding of the σ(C-O) orbital (red) and π(CH₃) orbitals (blue) with virtual orbitals in σ₁₁ and σ₂₂ are highlighted.
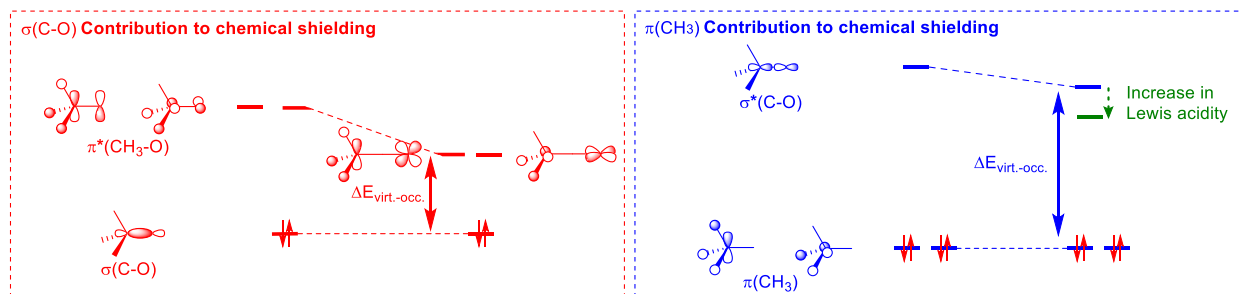
Figure S23. (Left) The σ(C-O) contribution through coupling with the $\pi*$(CH$_3$-O) orbitals by the angular momentum operator $\hat{L}_x$ and $\hat{L}_z$ leading to chemical shielding in σ_{11} and σ_{22}. (Right) The π(CH$_3$) contribution through coupling with the $\sigma*$(C-O) orbitals by the angular momentum operator $\hat{L}_x$ and $\hat{L}_z$ leading to chemical shielding in σ_{11} and σ_{22}. The decrease in energy of the $\sigma*$(C-O) orbital by increased Lewis acidity is highlighted in green.

Table S17. Isotropic and principal components of the chemical shift and shielding of the cluster models.

|	δ_{iso}[a] [ppm]	σ_{iso} [ppm]	σ_{11} [ppm]	σ_{22} [ppm]	σ_{33} [ppm]	σ_{11}[b] [ppm]	σ_{22}[b] [ppm]	σ_{33}[b] [ppm]
Ti-OCH$_3$	71	116	79	80	188	79	80	188
Nb-OCH$_3$	69	118	79	91	185	81	92	183
Ta-OCH$_3$	66	121	82	92	188	83	92	186
Zr-OCH$_3$	66	121	86	86	190	87	87	189
Hf-OCH$_3$	66	121	86	86	191	82	82	189

[a] Referenced to tetramethylsilane.
[b] Sum from NCS analysis

Table S18. Diamagnetic and paramagnetic chemical shielding contribution of the cluster models.

	$\sigma_{11\text{-dia}}$ [ppm]	$\sigma_{11\text{-para}}$ [ppm]	$\sigma_{22\text{-dia}}$ [ppm]	$\sigma_{22\text{-para}}$ [ppm]	$\sigma_{33\text{-dia}}$ [ppm]	$\sigma_{33\text{-para}}$ [ppm]
Ti-OCH$_3$						
Nb-OCH$_3$	225	-147	226	-146	230	-45
Ta-OCH$_3$	220	-137	217	-128	231	-46
Zr-OCH$_3$	221	-134	218	-127	230	-45
Hf-OCH$_3$	220	-135	220	-135	229	-42
Ti-OCH$_3$	216	-139	216	-139	229	-42

Table S19. NLMO contribution to the paramagnetic chemical shielding ($\sigma_{11\text{-para}}$) of the cluster models.

	$\sigma_{11\text{-para}}$ [ppm]	C-O [ppm]	Sum (C-H) [ppm]	C-H^1 [pmm]	C-H^2 [ppm]	C-H^3 [ppm]	M-O [ppm]	Rest [ppm]
Ti-OCH$_3$	-147	-89	-51	-55	3	1	-9	2
Nb-OCH$_3$	-137	-85	-48	3	0	-51	-11	6
Ta-OCH$_3$	-134	-83	-44	3	0	-47	-12	5
Zr-OCH$_3$	-135	-93	-32	18	-38	-12	-11	1
Hf-OCH$_3$	-139	-90	-27	-36	-10	19	-12	-10

Table S20. NLMO contribution to the paramagnetic chemical shielding ($\sigma_{22\text{-para}}$) of the cluster models.

	$\sigma_{22\text{-para}}$ [ppm]	C-O [ppm]	Sum (C-H) [ppm]	C-H^1 [ppm]	C-H^2 [ppm]	C-H^3 [ppm]	M-O [ppm]	Rest [ppm]
Ti-OCH$_3$	-146	-89	-50	21	-38	-33	-9	2
Nb-OCH$_3$	-128	-95	-27	-22	-20	15	0	-5
Ta-OCH$_3$	-127	-92	-27	-23	-18	15	0	-8
Zr-OCH$_3$	-135	-93	-32	-40	18	-10	-11	1
Hf-OCH$_3$	-139	-91	-26	17	-9	-35	-11	-11

XYZ Coordinates for Molecular Models

TMS

Si	0.0001166	0.0007625	-0.0002818
C	-0.0315924	1.2116905	1.4514412
H	0.8949666	1.7911615	1.5138922
H	-0.1543884	0.6917915	2.4068812
H	-0.8562544	1.9258295	1.3617112
C	-1.6235054	-0.9671875	-0.0477218
H	-1.7818114	-1.5332975	0.8756672
H	-1.6422394	-1.6838115	-0.8750288
H	-2.4848144	-0.3034285	-0.1733098
C	1.4432316	-1.2024235	0.2128682

H	1.3553636	-1.7779175	1.1398312
H	2.4034086	-0.6780315	0.2458472
H	1.4933046	-1.9205905	-0.6117198
C	0.2120466	0.9583435	-1.6165758
H	-0.6073534	1.6663175	-1.7764958
H	0.2357366	0.2878775	-2.4814498
H	1.1437846	1.5329145	-1.6255568

CH$_3$OH

C	0.2932617	-0.2062687	-0.0174933
O	-0.4993843	0.9093303	0.3545867
H	-0.1055683	-1.1538507	0.3698547

```
H    1.2803637   -0.0501317    0.4185547
H    0.4106117   -0.2947787   -1.1062583
H   -1.3792843    0.7956993   -0.0192443

[Si(OCH3)4]
Si   0.00012     0.00027     -0.00072
O    1.13835    -0.85474     -0.81512
O    0.79423     1.16030      0.84392
O   -0.83478    -1.07496      0.91420
O   -1.09747     0.76959     -0.94582
C   -2.16311     0.15223     -1.65747
H   -2.79454     0.94293     -2.06536
H   -2.76186    -0.48162     -0.99805
H   -1.78168    -0.45519     -2.48461
C    0.19633     2.27300      1.49777
H    0.99780     2.92831      1.84206
H   -0.39028     1.94972      2.36381
H   -0.45361     2.82780      0.81595
C   -0.26927    -2.11792      1.69914
H    0.27447    -1.71107      2.55790
H    0.41282    -2.73224      1.10546
H   -1.08663    -2.74098      2.06517
C    2.23568    -0.30784     -0.53634
H    2.80754     0.38722     -0.91590
H    1.89238     0.21650     -2.43405
H    2.88150    -1.13365     -1.83837

[Ti(OCH3)4]
Ti   0.0012607   0.0002940    0.0004729
O    0.5458897  -1.4000940    0.9857619
O   -0.4642153   1.3821010    1.0504139
O   -1.4290333  -0.4961980   -0.9671431
C   -2.1986303  -1.4965210   -1.5766801
H   -2.0987863  -2.4482270   -1.0418781
H   -1.8812203  -1.6424980   -2.6150661
H   -3.2538193  -1.2040280   -1.5747591
C   -1.4455603   2.1229450    1.7231239
H   -2.4107803   2.0532810    1.2081929
H   -1.1485463   3.1759760    1.7672059
H   -1.5668723   1.7538520    2.7475519
C    1.5723827  -2.1505540    1.5751859
H    1.2798867  -3.2047940    1.6214159
H    1.7647417  -1.7991480    2.5949049
H    2.4991497  -2.0701340    0.9953189
H    2.0105377   2.4696740   -1.1706611
C    2.0713627   1.5240550   -1.7218291
O    1.3513777   0.5154200   -1.0672921
H    3.1242337   1.2341170   -1.8024111
H    1.6766407   1.6804810   -2.7318281

[Ti(OCH3)4(CH3OH)]
Ti   0.2443627  -0.0530490    0.0277181
O    0.1300267  -1.5332570   -1.0957049
O   -0.2305493   1.5289360   -0.7456569
O    2.0324817   0.1216350    0.1528471
O   -2.0804873  -0.5762530   -0.2966539
C   -3.0380963   0.3318100   -0.8466039
H   -2.6512813   0.8245220   -1.7410849
H   -3.2276743   1.0874940   -0.0870049
H   -3.9713323  -0.1923080   -1.0732399
C    3.0329587   0.1449410    1.1407381
H    3.5849457   1.0896160    1.0923011
H    3.7397387  -0.6758230    0.9777921
H    2.5905527   0.0412930    2.1378961
C    0.4005687   2.7246170   -1.1271109
H    1.4921627   2.6295580   -1.0848099
H    0.0953307   3.5443160   -0.4658869
H    0.1147377   2.9871430   -2.1523779
C    1.0844927  -2.3601540   -1.7197489
H    0.9205777  -2.3721290   -2.8036649
H    0.9958737  -3.3876820   -1.3477129
H    2.1029907  -2.0053830   -1.5271879
H   -2.0702713  -0.8692650    2.2599991
C   -1.1435183  -0.5389740    2.7391471
O   -0.1717873  -0.2396020    1.7742381
H   -0.7831963  -1.3359340    3.3993541
H   -1.3547153   0.3463210    3.3499031
H   -1.8388913  -1.2623880   -0.9374859
```

```
[Ti(OCH3)4]2
Ti   0.8976559   0.8565690   -1.1014163
O    0.5911229   2.4257720   -1.9579473
O    0.8223369  -0.8613280    0.1738357
O    1.0994089  -0.2394160   -2.5309353
O    2.4420449   1.3450490   -0.3015483
C    3.2261319   1.2707880    0.8590787
H    4.2347669   0.9240860    0.6082537
H    2.7847159   0.5816130    1.5876237
H    3.3076779   2.2600530    1.3225787
C    1.3445189  -0.1040150   -3.9086633
H    2.4101019  -0.2442610   -4.1234893
H    1.0406489   0.8873930   -4.2640283
H    0.7781299  -0.8642770   -4.4570023
C    1.7709759  -1.9159670    0.0657887
H    1.6217659  -2.4540230   -0.8738823
H    1.6587259  -2.5994960    0.9086127
H    2.7818669  -1.4993790    0.0687597
C    1.0704129   3.7440130   -1.9884603
H    1.2357969   4.0575810   -3.0249253
H    2.0154679   3.8213710   -1.4381213
H    0.3413659   4.4271840   -1.5367483
H   -1.6217271   2.4537990    0.8750187
H   -2.4105241   0.2452360    4.1230297
H   -1.2321341  -4.0603760    3.0223017
H   -4.2351481  -0.9246000   -0.6087903
Ti  -0.8976471  -0.8559750    1.1018607
C   -1.0703321  -3.7441130    1.9860937
C   -3.2260181  -1.2708630   -0.8582253
C   -1.3449171   0.1033860    3.9094207
C   -1.7707911   1.9165830   -0.0651583
O   -0.8225371   0.8616440   -0.1737213
O   -0.5910841  -2.4258120    1.9574007
O   -1.0979011   0.2393110    2.5320527
O   -2.4431271  -1.3433520    0.3033197
H   -1.6579191   2.6007860   -0.9073543
H   -1.0430831  -0.8887730    4.2643997
H   -0.3429101  -4.4261690    1.5300677
H   -3.3064461  -2.2606360   -1.3208553
H   -2.7818641   1.5003900   -0.0689303
H   -2.0172721  -3.8200290    1.4387997
H   -2.7843611  -0.5820850   -1.5870133
H   -0.7779121   0.8623390    4.4589197

[Zr(OCH3)4]2
Zr  -1.8094718   0.1552768   -0.0395852
O   -3.0238448  -1.3038322    0.4880798
O    0.1392022   1.2296618   -0.0935352
O   -2.3286158   0.5340358   -1.8881252
O   -2.4929958   1.5568988    1.1635648
C   -3.2136258   2.2449778    2.1403608
H   -3.7637748   3.0825918    1.6942978
H   -2.5405928   2.6487098    2.9068278
H   -3.9383738   1.5860128    2.6351128
C   -3.1202098   0.6884828   -3.0294642
H   -3.5975248   1.6756568   -3.0403512
H   -3.9064108  -0.0753382   -3.0685992
H   -2.5043998   0.5950638   -3.9312272
C    0.2082502   2.6482358   -0.2225562
H    0.1238372   2.9370428   -1.2752932
H    1.1585092   3.0157828    0.1685888
H   -0.6130088   3.1019388    0.3364448
C   -3.8304138  -2.2887742    1.0544738
H   -4.5019238  -2.7185522    0.3010428
H   -4.4461428  -1.8734642    1.8619438
H   -3.2248028  -3.1024492    1.4741678
H   -0.1289608  -2.9371402    1.2755338
H    3.5942892  -1.6687872    3.0483078
H    4.5043502   2.7157758   -0.3104492
H    3.7638032  -3.0871842   -1.6876342
Zr   1.8097602  -0.1554312    0.0396988
C    3.8299742   2.2859228   -1.0612662
C    3.2149052  -2.2497402   -2.1354952
C    3.1193862  -0.6805392    3.0315398
C   -0.2083858  -2.6485022    0.2223668
O   -0.1389248  -1.2299262    0.0934048
O    3.0236562   1.3029738   -0.4910232
O    2.3287582  -0.5308152    1.8889078
O    2.4943262  -1.5592612   -1.1603862
H   -1.1567968  -3.0163162   -0.1732362
```

```
H    3.9074172    0.0815868    3.0667008
H    3.2242822    3.0998878   -1.4802822
H    3.9407192   -1.5923772   -2.6308182
H    0.6155672   -3.1021442   -0.3326692
H    4.4426792    1.8685858   -1.8699912
H    2.5420352   -2.6540582   -2.9018072
H    2.5033412   -0.5804712    3.9324308

[Hf(OCH3)4]2
Hf  -1.8026489    0.0669080    0.0612837
O   -2.5582479    1.2944210   -1.2794233
O   -0.0766969   -1.2366270    0.0216107
O   -2.2998949    0.6263780    1.8661627
O   -2.9706259   -1.4823250   -0.2614453
C   -3.7866539   -2.5363670   -0.6646293
H   -4.5678329   -2.7284680    0.0810267
H   -3.2057299   -3.4592310   -0.7918533
H   -4.2761129   -2.3117890   -1.6204933
C   -3.0719299    0.8363870    3.0113137
H   -2.4340319    0.8417090    3.9024677
H   -3.8231279    0.0461340    3.1313337
H   -3.5921139    1.8002050    2.9571637
C   -0.0745919   -2.6651200    0.0374087
H    0.7624241   -3.0153010    0.6444467
H    0.0341381   -3.0513120   -0.9807053
H   -1.0101589   -3.0352600    0.4590117
C   -3.4282239    1.7992680   -2.2467783
H   -3.8997939    2.7252610   -1.8951733
H   -4.2235899    1.0803980   -2.4814953
H   -2.8874309    2.0246820   -3.1740023
H   -0.7630749    3.0146510   -0.6423163
H    3.2065431    3.4595870    0.7874587
H    2.4330941   -0.8285460   -3.9028703
H    4.2235791   -1.0814520    2.4833677
Hf   1.8026481   -0.0676700   -0.0604081
C    3.0709021   -0.8337510   -3.0116433
C    3.4288121   -1.8004920    2.2471507
C    3.7868951    2.5359370    0.6633617
C    0.0747871    2.6644170   -0.0364913
O    0.0767061    1.2359080   -0.0205923
O    2.2999621   -0.6285220   -1.8648753
O    2.9707901    1.4818410    0.2604597
O    2.5579781   -1.2940210    1.2814387
H   -0.0323529    3.0507000    0.9817547
H    4.2740461    2.3128220    1.6207477
H    3.5856021   -1.8008840   -2.9649483
H    3.9011421   -2.7251650    1.8930787
H    1.0097841    3.0343900   -0.4595073
H    3.8265811   -0.0468540   -3.1254483
H    2.8885701   -2.0286940    3.1740097
H    4.5698811    2.7258460   -0.0809563

[Nb(OCH3)5]2
Nb  -2.0756804   -0.3721039    0.1105541
O   -3.2309774   -0.0805729    1.6216131
O   -0.2653374   -0.3900669   -1.1537429
O   -1.7550974   -2.2187509    0.4704931
O   -2.1505024    1.5357221   -0.2785259
C   -1.5775604    2.6511531   -0.9077089
H   -0.5188464    2.7369851   -0.6514539
H   -2.1014584    3.5601321   -0.5907509
H   -1.6654604    2.5670791   -1.9979919
C   -1.0996544   -3.4124249    0.7871681
H   -1.4619834   -3.7825999    1.7525281
H   -0.0208234   -3.2476829    0.8404151
H   -1.3137734   -4.1675369    0.0224281
C   -0.2146854   -1.1977319   -2.3307989
H    0.5711956   -0.8288899   -2.9915009
H   -1.1788034   -1.1565259   -2.8390149
H    0.0047776   -2.2362119   -2.0666329
C   -3.9551214    0.9823761    2.1887551
H   -3.7433664    1.9166511    1.6574921
H   -3.6858664    1.0935301    3.2441901
H   -5.0266834    0.7663951    2.1265081
H    0.6788426    0.9734331    2.8824511
H    2.8125056   -1.8604309    2.3243801
H    2.9466726    2.6151991    1.4159381
H    3.6443466   -2.9231869    0.2579361
Nb   1.4811316   -0.0277719    0.0300721
C    2.4821306    2.9158061    0.4698721

C    2.8225206   -2.8251189   -0.4617669
C    3.1381606   -0.8389709    2.5471501
C   -0.3178894    0.8793841    2.4504031
O   -0.2515604    0.0916431    1.2641041
O    1.5924966    1.9224271    0.0393321
O    2.6337706    0.0749511    1.6074851
O    1.8349986   -1.9497269    0.0106991
H   -0.7027884    1.8767981    2.2177641
H    4.2334226   -0.8038619    2.5437961
H    1.9400886    3.8563741    0.6162211
H    3.2301736   -2.4506219   -1.4075429
H   -0.9852904    0.3947911    3.1665021
H    3.2757536    3.0847801   -0.2680069
H    2.3870846   -3.8173389   -0.6235839
H    2.7914606   -0.5722269    3.5523341
O   -3.2595194   -0.7251449   -1.3732479
C   -4.0336854    0.0184151   -2.2799499
H   -3.9677864    1.0902491   -2.0641739
H   -5.0794014   -0.2976929   -2.2078369
H   -3.6897774   -0.1644109   -3.3042029
O    2.5930906    0.0156991   -1.5794629
C    2.9762526    0.9890641   -2.5160769
H    2.7158356    0.6573121   -3.5278759
H    4.0617916    1.1350311   -2.4753779
H    2.4808776    1.9462241   -2.3213579

[Ta(OCH3)5]2
Ta  -2.0627243   -0.0424314    0.0881402
O   -3.1867373   -0.9346954    1.3758972
O   -0.2732163    0.5844586   -1.0064798
O   -1.9322623   -1.6775534   -0.9464998
O   -2.0317423    1.6445526    1.0294132
C   -1.4897753    2.7722636    1.6532972
H   -0.4205633    2.8451436    1.4402502
H   -1.6344903    2.7027926    2.7374612
H   -1.9908313    3.6809686    1.2993852
C   -1.5008263   -2.2865934   -2.1280178
H   -0.5621763   -1.8408344   -2.4710348
H   -2.2605163   -2.1647814   -2.9096868
H   -1.3385013   -3.3568374   -1.9621908
C   -0.2847643    1.5479986   -2.0612778
H    0.5122597    1.3195906   -2.7703628
H   -0.1277082    2.5516566   -1.6544908
H   -1.2471513    1.5121406   -2.5726118
C   -3.8206943   -2.1829604    1.5230062
H   -3.5328913   -2.6341844    2.4782712
H   -3.5417563   -2.8560804    0.7056382
H   -4.9061833   -2.0423804    1.5203402
H    0.6533987   -1.2644154    2.9015032
H    2.9995937   -2.6292584    1.3470022
H    3.0733847    1.7663576    2.3108622
H    3.0055097   -3.2763194   -1.1274598
Ta   1.4966867   -0.0308414    0.0376972
C    2.4916797    2.4674406    1.7024162
C    2.3231547   -2.5905274   -1.6431778
C    3.4103237   -1.7407174    1.8383922
C   -0.2135633   -1.4809304    2.2763912
O   -0.2337313   -0.5825414    1.1650142
O    1.6837637    1.7668006    0.7958892
O    2.7080847   -0.5809664    1.4672682
O    1.5981497   -1.8238454   -0.7226548
H   -1.1250783   -1.3515584    2.8603992
H    4.4657317   -1.6415204    1.5606112
H    1.8654787    3.0775286    2.3635402
H    2.9079347   -1.9379786   -2.3016618
H   -0.1547603   -2.5141954    1.9207092
H    3.1812287    3.1366306    1.1742442
H    1.6353247   -3.1885834   -2.2507018
H    3.3543727   -1.8771314    2.9236052
O   -3.2961653    0.7065696   -1.2103368
C   -4.0547933    1.8820076   -1.3516288
H   -3.7938453    2.6142106   -0.5800718
H   -5.1201613    1.6430496   -1.2676678
H   -3.8793623    2.3215606   -2.3395648
O    2.6420397    0.4995946   -1.4545258
C    3.3531817    1.6434776   -1.8558638
H    3.2447707    1.7885266   -2.9360418
H    4.4188177    1.5161806   -1.6339608
H    2.9921087    2.5391616   -1.3387168
```

XYZ coordinates of the silica cluster models

[CH₃O-Ti@SiO₂]

O	1.1141761	3.1010477	0.6419320
Si	2.4459311	-0.1399373	-1.0041130
Si	-1.9500939	1.3457717	2.0024140
O	0.8574811	-1.1575853	2.4034490
O	-0.6222359	2.1984367	2.4443410
O	-1.6509579	-0.2494523	2.2446360
Si	-0.6835889	-1.5566843	2.0010150
O	-1.6050589	-0.0634443	-1.5359170
Si	0.9423571	2.6118037	2.1982940
O	-0.7483809	-1.9716163	0.4237180
O	1.8941991	1.2978977	2.4565320
O	2.7110361	-0.4471283	0.5896090
Si	-1.8356609	1.5142477	-1.1644490
O	1.1601791	-1.0525483	-1.4808050
Ti	-0.5712779	-1.5430783	-1.3223430
O	-2.2683879	1.6361277	0.4161740
H	-3.0990529	1.7516187	2.8062330
Si	2.2218061	-0.2819363	2.1482940
H	3.2785771	-0.7485893	3.0392170
O	-0.4261619	2.3249017	-1.4076270
O	2.0852821	1.4428897	-1.2069410
H	3.6410201	-0.4753843	-1.7749810
Si	1.0964421	2.7291507	-0.9547430
H	-2.8854319	2.1028467	-1.9970590
H	-1.1339499	-2.6632903	2.8531740
H	1.3323741	3.6882717	3.1036530
H	1.5688521	3.8661457	-1.7371560
O	-1.0246939	-2.8524043	-2.4103060
C	-1.3855359	-3.8944093	-3.2761420
H	-1.6647709	-4.7810973	-2.6938050
H	-0.5481559	-4.1491803	-3.9343990
H	-2.2463159	-3.5833903	-3.8808990

[CH₃O-Zr@SiO₂]

O	-3.0325286	0.3464980	1.5047240
Si	0.0228054	-1.9664740	1.8512010
Si	-1.7672146	1.8798520	-1.7691170
O	-0.8591596	-1.8344770	-1.9469700
O	-3.0360216	1.1186060	-1.0555040
O	-0.8577716	0.7709170	-2.5658530
Si	0.0185044	-0.6202560	-2.6268510
O	1.3889244	1.7206760	0.5159130
Si	-3.5940776	-0.0054060	0.0029390
O	1.3970744	-0.4156690	-1.7597340
O	-3.0432356	-1.4861420	-0.4439800
O	-0.8625446	-2.6092260	0.6224290
Si	0.0177564	2.5845850	0.7766920
O	1.3968044	-1.3171180	1.2305670
Zr	2.2203164	-0.0018760	-0.0037140
O	-0.8630476	2.6130610	-0.6127790
H	-2.2594546	2.8796110	-2.7128870
Si	-1.7662516	-2.4766940	-0.7404780
H	-2.2488706	-3.7961330	-1.1385260
O	-0.8612796	1.8411350	1.9522720
O	-0.8499886	-0.7711970	2.5699680
H	0.3200154	-3.0090460	2.8332270
Si	-1.7620036	0.5915250	2.5168630
H	0.3191834	3.9553420	1.1880060
H	0.3082724	-0.9514400	-4.0218470
H	-5.0539876	-0.0014600	0.0060860
H	-2.2514936	0.9064810	3.8561950
O	4.1620964	0.0042960	-0.0033230
C	5.5666694	0.0111170	-0.0060480
H	5.9427064	-0.2148950	-1.0085210
H	5.9485744	-0.7405730	0.6913870
H	5.9392264	0.9943800	0.2968630

[CH₃O-Hf@SiO₂]

O	-3.0399139	0.0799347	-1.5596731
Si	0.0131371	2.4160747	-1.2023231
Si	-1.7537889	-2.3231952	1.1433669
O	-0.8783649	1.1874837	2.4034769
O	-3.0265879	-1.3982903	0.6710429
O	-0.8588349	-1.4851973	2.2337509
Si	0.0118461	-0.1661683	2.6915239
O	1.4087271	-1.4928933	-0.9946831
Si	-3.5936339	-0.0198953	-0.0169891

O	1.3827641	-0.0997283	1.7934169
O	-3.0436959	1.2702727	0.8362339
O	-0.8668059	2.6692517	0.1648079
Si	0.0401321	-2.2478453	-1.4918631
O	1.3909711	1.6202027	-0.8041811
Hf	2.2166171	0.0130007	0.0032119
O	-0.8370249	-2.6819173	-0.1691471
H	-2.2398749	-3.5575002	1.7538209
Si	-1.7809499	2.1431597	1.4214569
H	-2.2805679	3.2882508	2.1775249
O	-0.8453289	-1.1981243	-2.3978241
O	-0.8617259	1.4792137	-2.2338951
H	0.3032281	3.7006087	-1.8388281
Si	-1.7586629	0.1514987	-2.5859751
H	0.3451231	-3.4382043	-2.2851681
H	0.3130741	-0.2545753	4.1200199
H	-5.0535159	-0.0296133	-0.0160271
H	-2.2358959	0.2334337	-3.9636711
O	4.1564241	0.0224307	0.0172219
C	5.5598411	0.0283927	0.0297999
H	5.9289611	-0.0514943	1.0568339
H	5.9378091	0.9572538	-0.4081061
H	5.9465181	-0.8158222	-0.5491561

[CH₃O-Nb@SiO₂]

O	-3.4577038	0.4071864	2.1186777
Si	-0.7353468	-2.2193856	2.8938587
Si	-2.2726548	0.9119064	-1.1750563
O	-1.4681438	-2.9480406	-0.9211123
O	-3.7482418	0.7855204	-0.4970523
O	-1.8063248	-0.5347826	-1.7300633
Si	-0.6314858	-1.6436926	-1.4734263
O	1.0175472	0.8448324	1.5481997
Si	-4.1347148	-0.2259026	0.7597747
O	0.4362592	-1.2410226	-0.3062253
O	-3.5197398	-1.7148206	0.4360357
O	-1.6702598	-2.9973296	1.7892817
Si	-0.2368488	1.8606654	1.1584037
O	0.7738692	-2.0275306	2.2827177
Nb	1.7517452	-0.8254746	1.0933527
O	-1.1601028	1.2438214	-0.0237823
Si	-2.5079228	-3.0170346	0.3780487
H	-3.2774948	-4.2518006	0.2635257
O	-1.1957008	1.9032154	2.4826517
O	-1.3336248	-0.7115186	3.2061427
H	-0.7123128	-2.9976576	4.1318937
Si	-2.1715328	0.6925914	3.1011477
H	-5.5851268	-0.2873276	0.9076497
H	-2.6324998	1.1422504	4.4106057
O	3.3403762	-1.0762656	2.1093647
C	4.7428262	-1.1703106	2.0313217
H	5.0570892	-2.1981246	2.2316027
H	5.1823682	-0.5102376	2.7833807
H	5.0767802	-0.8680016	1.0338237
O	2.9830942	-0.3381856	-0.3763203
O	0.1825042	-1.6592106	-2.9017823
Si	3.0480452	0.7086084	-1.6303993
Si	0.8847352	-0.3694316	-3.6872973
O	2.2725492	0.0717844	-2.9323753
O	2.3170182	2.1115914	-1.1490463
H	4.4331032	0.9966624	-2.0070693
O	-0.0813518	0.9680974	-3.6735643
H	1.1602162	-0.7821136	-5.0598523
O	-2.1747188	2.0127704	-2.3719283
O	0.4607462	3.1913884	0.5121267
Si	1.2433212	3.3341764	-0.9608973
Si	-0.7957008	2.3761254	-3.2190793
O	0.1817432	3.2339864	-2.2117713
H	1.9023742	4.6363364	-0.9691013
H	-1.1387168	3.1816844	-4.3863853

[CH₃O-Ta@SiO₂]

O	-3.4573459	0.4138564	2.1182657
Si	-0.7435219	-2.2183666	2.8997277
Si	-2.2693949	0.9057924	-1.1735783
O	-1.4782839	-2.9564496	-0.9252893
O	-3.7455589	0.7835204	-0.4965183
O	-1.8050019	-0.5417376	-1.7291093
Si	-0.6356079	-1.6576766	-1.4819833
O	1.0265821	0.8331004	1.5388817

Si	-4.1344659	-0.2240096	0.7619997
O	0.4446121	-1.2750126	-0.3192353
O	-3.5216119	-1.7139056	0.4381557
O	-1.6719329	-2.9966466	1.7886457
Si	-0.2244069	1.8502274	1.1542417
O	0.7621051	-2.0170056	2.2907577
Ta	1.7594361	-0.8464236	1.0775487
O	-1.1516799	1.2312694	-0.0255223
Si	-2.5128989	-3.0185686	0.3796977
H	-3.2853869	-4.2519436	0.2697357
O	-1.1847749	1.8985504	2.4776667
O	-1.3442769	-0.7119196	3.2120837
H	-0.7265409	-3.0001686	4.1354197
Si	-2.1701869	0.6980124	3.1001857
H	-5.5848879	-0.2840856	0.9100407
H	-2.6293929	1.1575754	4.4068347
O	3.3478361	-1.1203366	2.1011577
C	4.7548201	-1.1637486	2.0689817
H	5.0983531	-2.1828726	2.2649497

H	5.1487841	-0.5020926	2.8444837
H	5.1149491	-0.8354166	1.0889717
O	2.9801691	-0.3054566	-0.3836873
O	0.1761161	-1.6650966	-2.9121353
Si	3.0504291	0.7260684	-1.6478403
Si	0.8786261	-0.3715036	-3.6928573
O	2.2639151	0.0738914	-2.9359753
O	2.3316941	2.1377924	-1.1757073
H	4.4341611	1.0019544	-2.0370613
O	-0.0895319	0.9642344	-3.6788123
H	1.1572671	-0.7828686	-5.0651793
O	-2.1765509	2.0073704	-2.3693923
O	0.4673751	3.1820824	0.5033547
Si	1.2407471	3.3425784	-0.9720903
Si	-0.8024389	2.3727034	-3.2230383
O	0.1761341	3.2334254	-2.2198763
H	1.8824531	4.6532794	-0.9765873
H	-1.1508829	3.1760284	-4.3903103

Section S10. ATR-IR spectra and solution ^1H, ^{13}C, and ^1H-^{13}C HSQC NMR spectra of $[Nb(OCH_3)_5]_2$ and $[Ta(OCH_3)_5]_2$. CP-MAS ^{13}C-NMR spectrum for $[Ti(OCH_3)_4]_2$.

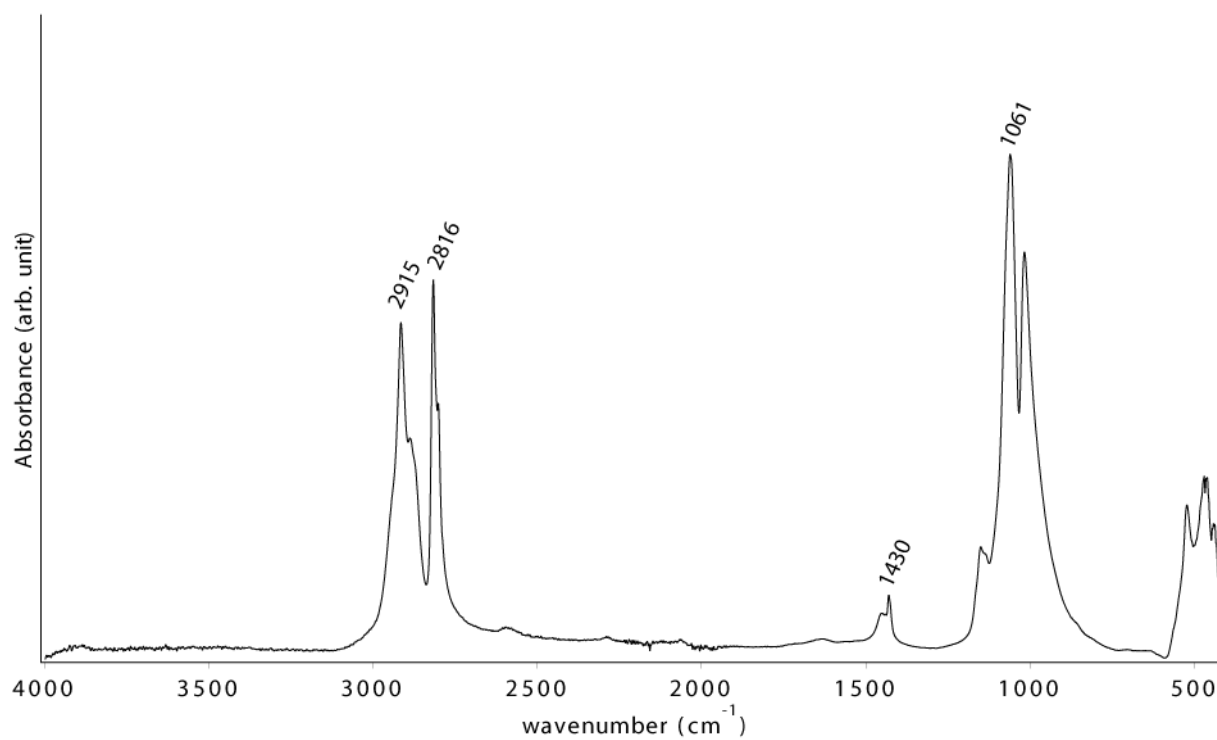**Figure S24.** ATR-IR spectrum of $[Nb(OCH_3)_5]_2$ (298 K, under inert atmosphere).

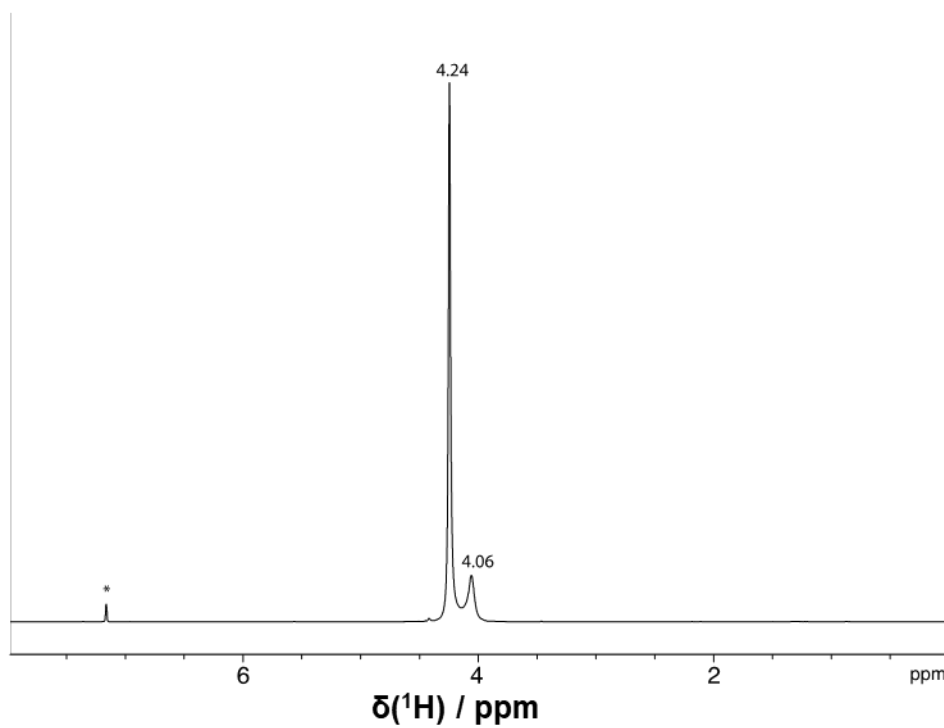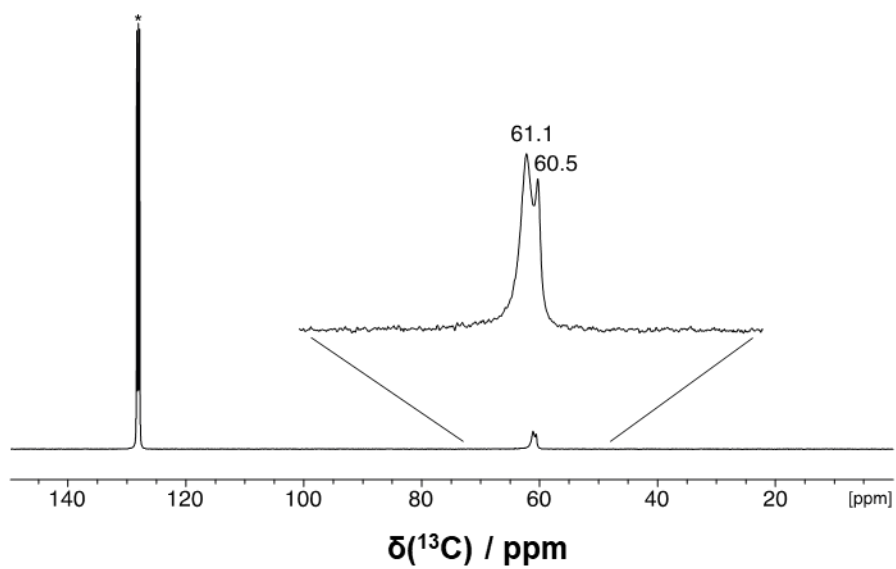**Figure S25.** Solution ^1H NMR spectrum of $[Nb(OCH_3)_5]_2$ (C_6D_6).

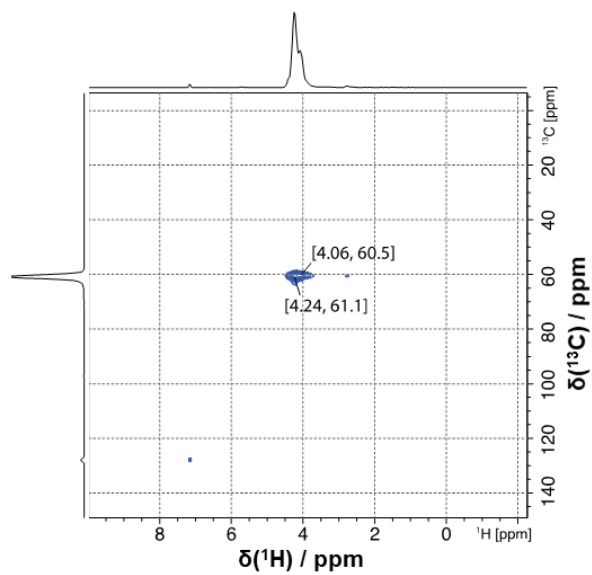**Figure S26.** Solution ^{13}C NMR spectrum of $[Nb(OCH_3)_5]_2$ (C_6D_6).

Figure S27. Solution ^1H-^{13}C HSQC NMR spectrum of $[Nb(OCH_3)_5]_2$ (C_6D_6).

S37
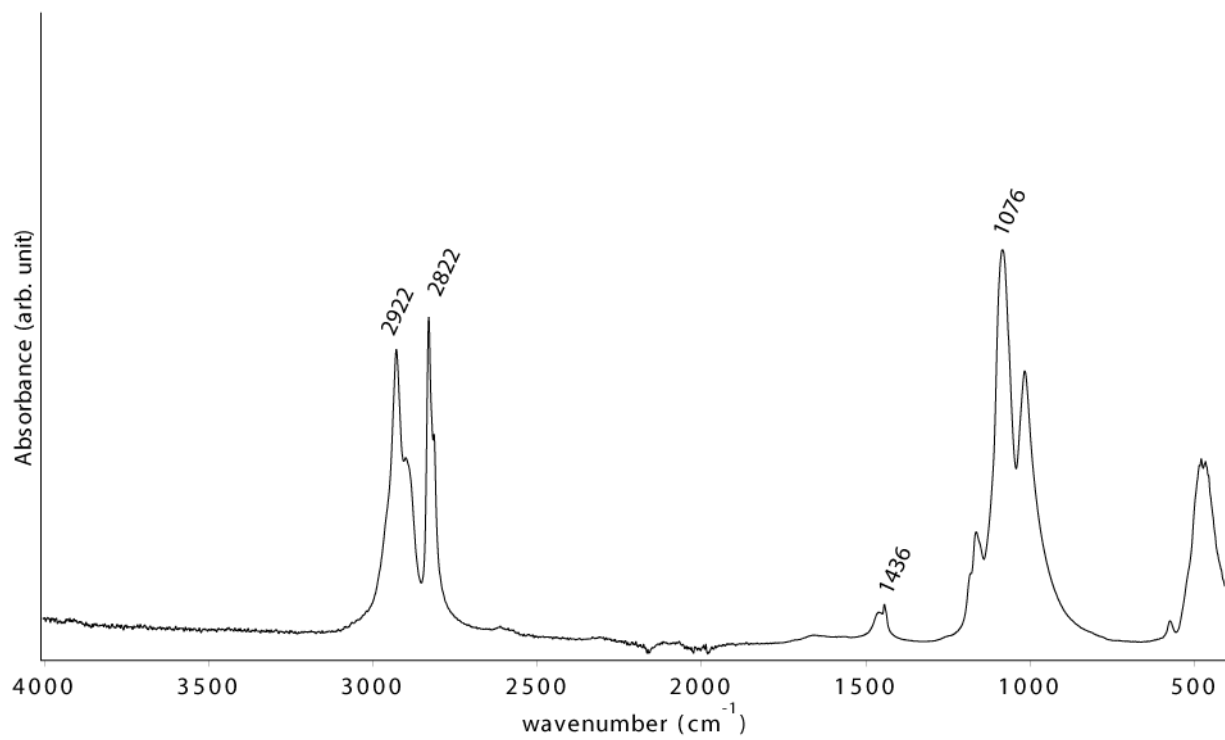
Figure S28. ATR-IR spectrum of [Ta(OCH$_3$)$_5$]$_2$ (298 K, under inert atmosphere).
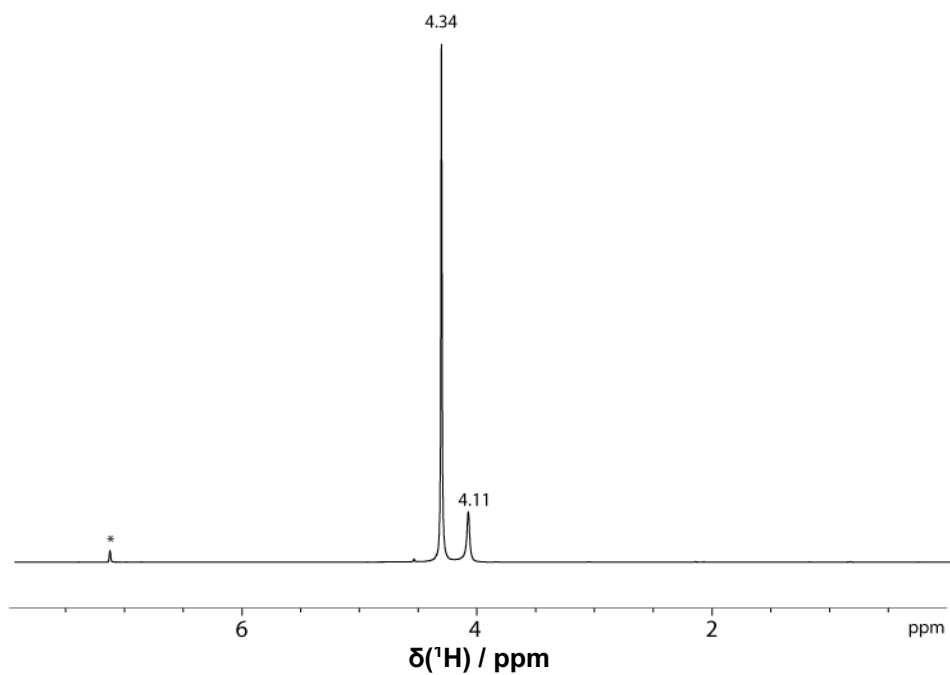
Figure S29. Solution ^{1}H NMR spectrum of [Ta (OCH$_3$)$_5$]$_2$ (C$_6$D$_6$).
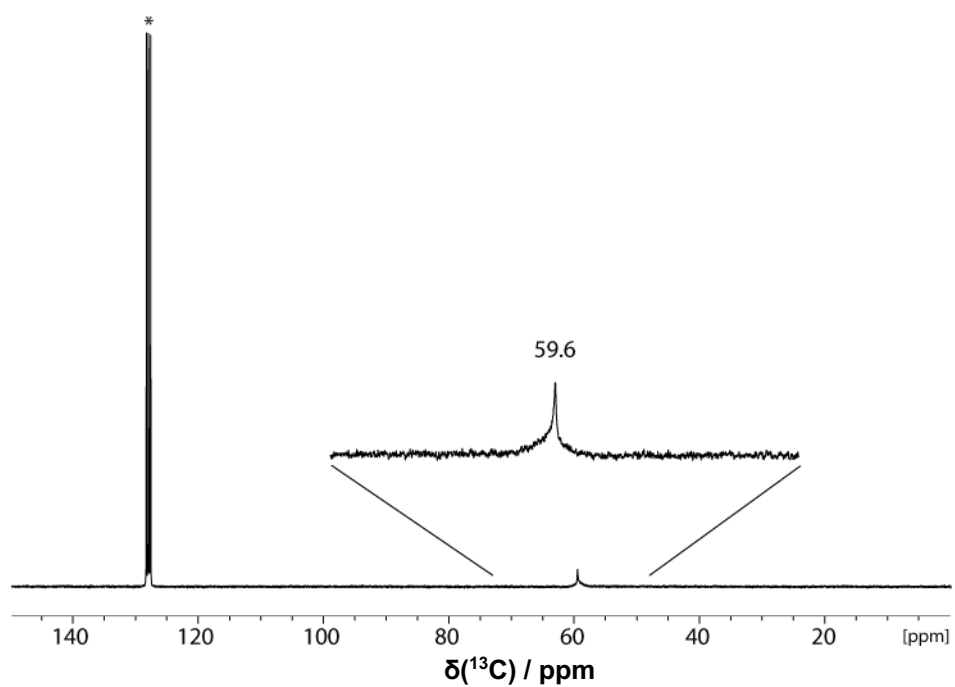
Figure S30. Solution ^{13}C NMR spectrum of $[Ta(OCH_3)_5]_2$ (C_6D_6).
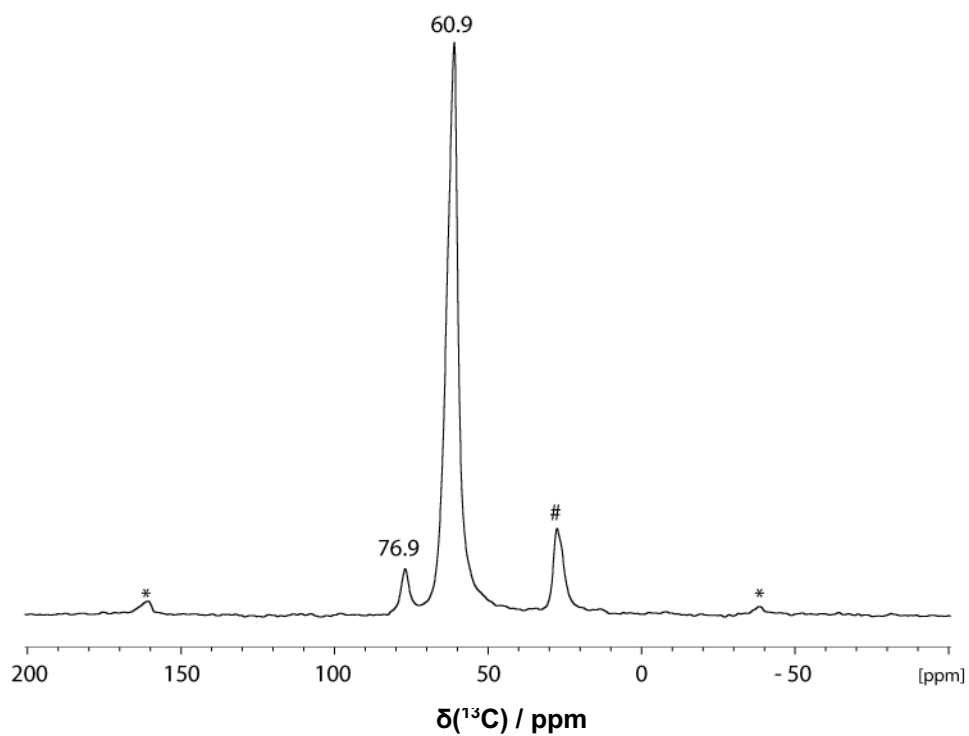
Figure S31. Solid state CP-MAS ^{13}C NMR spectrum of $[Ti(OCH_3)_4]_2$ (spinning rate = 10 kHz).
* denotes spinning sidebands; # denotes an unknown impurity in the as-purchased compound.

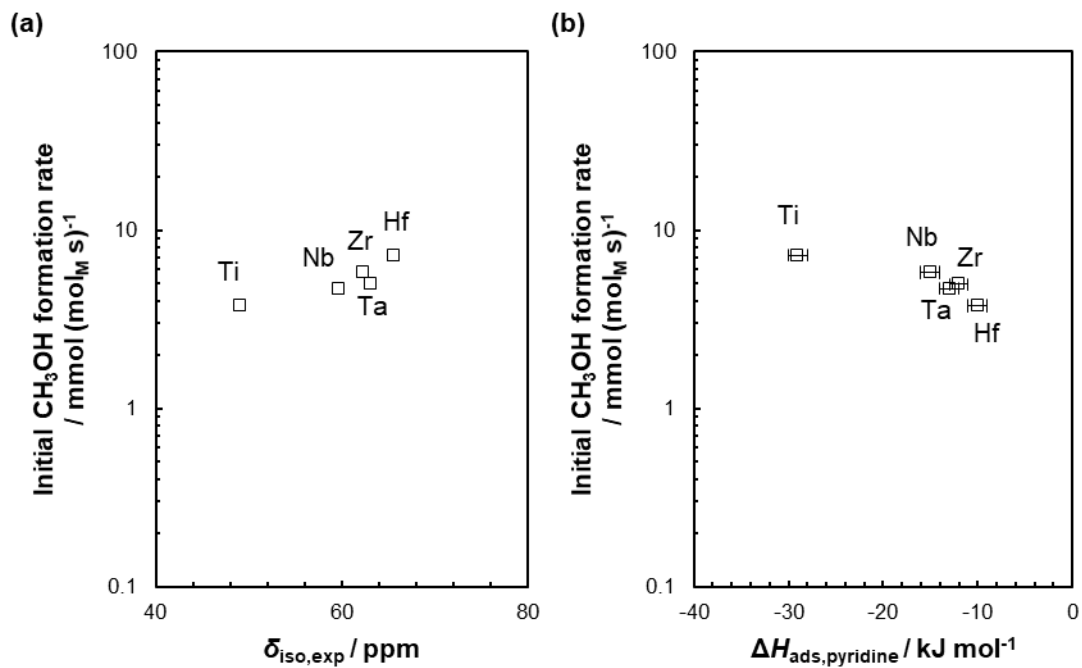**Section S11. CH₃OH formation rates as a function of pyridine adsorption enthalpies for Cu/M@SiO₂**

Figure S32. Initial CH₃OH formation turnover rate, normalized by moles of M, for Cu/M@SiO₂ as a function of **(a)** the ^{13}C chemical shift for methoxy intermediates ($\delta_{iso,exp}$) and **(b)** the pyridine adsorption enthalpy for M@SiO₂. Note the logarithmic scale. Error bars in the y-value are smaller than the size of the data point.

References

[1]   T. Tsuda, T. Hashimoto and T. Saegusa, *J. Am. Chem. Soc.*, 1972, **94**, 658–659.
[2]   G. Takahiro, K. Takayuki and A. Yoshimoto, *J. Sol-Gel Sci. Technol.*, 1998, **13**, 975–979.
[3]   K. W. Terry, C. G. Lugmair and T. D. Tilley, *J. Am. Chem. Soc.*, 1997, **119**, 9745–9756.
[4]   C. G. Lugmair and T. Don Tilley, *Monatshefte fur Chemie*, 2006, **137**, 557–566.
[5]   D. C. Bradley, B. N. Chakravarti and W. Wardlaw, *J. Chem. Soc.*, 1956, 2381.
[6]   D. C. Bradley, W. Wardlaw and A. Whitley, *J. Chem. Soc.*, 1955, 726.
[7]   R. L. Brutchey, C. G. Lugmair, L. O. Schebaum and T. D. Tilley, *J. Catal.*, 2005, **229**, 72–81.
[8]   B. O. Wagner and G. S. Hammond, *J. Organomet. Chem.*, 1975, **85**, 1–14.
[9]   J. Wang, V. F. Kispersky, W. Nicholas Delgass and F. H. Ribeiro, *J. Catal.*, 2012, **289**, 171–178.
[10]   O. Müller, M. Nachtegaal, J. Just, D. Lützenkirchen-Hecht, R. Frahm, *J. Synchrotron Radiat.* **2016**, *23*, 260–266.
[11]   A. H. Clark, J. Imbao, R. Frahm, M. Nachtegaal, *J. Synchrotron Radiat.* **2020**, *27*, 551–557.
[12]   B. Ravel, M. Newville, *J. Synchrotron Radiat.* **2005**, *12*, 537–541.
[13]   A. D. Becke, *J. Chem. Phys.*, 1993, **98**, 5648–5652.
[14]   R. Krishnan, J. S. Binkley, R. Seeger and J. A. Pople, *J. Chem. Phys.*, 1980, **72**, 650–654.
[15]   A. D. McLean and G. S. Chandler, *J. Chem. Phys.*, 1980, **72**, 5639–5648.
[16]   M. Dolg, U. Wedig, H. Stoll and H. Preuss, *J. Chem. Phys.*, 1987, **86**, 866–872.
[17]   D. Andrae, U. Häußermann, M. Dolg, H. Stoll and H. Preuß, *Theor. Chim. Acta*, 1990, **77**, 123–141.
[18]   M. J.Frisch, G. W.Trucks, H. B.Schlegel, G. E.Scuseria, M. A.Robb, J. R.Cheeseman, G.Scalmani, V.Barone, B.Mennucci, G. A.Petersson,
        H.Nakatsuji, M.Caricato, X.Li, H. P.Hratchian, A. F.Izmaylov, J.Bloino, G.Zheng, J. L.Sonnenberg, M.Hada, M.Ehara, K.Toyota, R.Fukuda,
        J.Hasegawa, M.Ishida, T.Nakajima, Y.Honda, O.Kitao, H.Nakai, T.Vreven, J. J. A.Montgomery, J. E.Peralta, F.Ogliaro, M.Bearpark, J.
        J.Heyd, E.Brothers, K. N.Kudin, V. N.Staroverov, R.Kobayashi, J.Normand, K.Raghavachari, A.Rendell, J. C.Burant, S. S.Iyengar, J.Tomasi,
        M.Cossi, N.Rega, J. M.Millam, M.Klene, J. E.Knox, J. B.Cross, V.Bakken, C.Adamo, J.Jaramillo, R.Gomperts, R. E.Stratmann, O.Yazyev, A.
        J.Austin, R.Cammi, C.Pomelli, J. W.Ochterski, R. L.Martin, K.Morokuma, V. G.Zakrzewski, G. A.Voth, P.Salvador, J. J.Dannenberg,
        S.Dapprich, A. D.Daniels, Ö.Farkas, J. B.Fore, J.Cioslowski and D. J.Fox, Gaussian 09, Revision D.01, Gaussian, Inc., Wallingford CT, 2009
[19]   R. Ditchfield, *Mol. Phys.*, 1974, **27**, 789–807.
[20]   K. Wolinski, J. F. Hinton and P. Pulay, *J. Am. Chem. Soc.*, 1990, **112**, 8251–8260.
[21]   G. te Velde, F. M. Bickelhaupt, E. J. Baerends, C. Fonseca Guerra, S. J. A. van Gisbergen, J. G. Snijders and T. Ziegler, *J. Comput. Chem.*,
        2001, **22**, 931–967.
[22]   Amsterdam Density Functional (ADF) Theoretical Chemistry Vrieje Universitet see http://www.scm.com (Version 2014).
[23]   E. Van Lenthe and E. J. Baerends, *J. Comput. Chem.*, 2003, **24**, 1142–1156.
[24]   Y. Zhang and W. Yang, *Phys. Rev. Lett.*, 1998, **80**, 890–890.
[25]   E. van Lenthe, R. van Leeuwen, E. J. Baerends and J. G. Snijders, *Int. J. Quantum Chem.*, 1996, **57**, 281–293.
[26]   J. A. Bohmann, F. Weinhold and T. C. Farrar, *J. Chem. Phys.*, 1997, **107**, 1173–1184.
[27]   J. Autschbach, *J. Chem. Phys.*, 2008, **128**, 164112.
[28]   E. D. Glendening, J. K. Badenhoop, A. E. Reed, J. E. Carpenter, J. A. Bohmann, C. M. Morales, C. R. Landis, F. Weinhold, Theoretical
        Chemistry Institute, University of Wisconsin, Madison, WI, USA 2013, http://nbo6.chem.wisc.edu/
[29]   E. Zurek, C. J. Pickard and J. Autschbach, *J. Phys. Chem. C*, 2008, **112**, 11744–11750.
[30]   J. Autschbach, S. Zheng and R. W. Schurko, *Concepts Magn. Reson. Part A*, 2010, **36A**, 84–126.
        https://ja01.chem.buffalo.edu/tutorials/tensorgraphics.html
[31]   G. R. Fulmer, A. J. M. Miller, N. H. Sherden, H. E. Gottlieb, A. Nudelman, B. M. Stoltz, J. E. Bercaw and K. I. Goldberg, *Organometallics*,
        2010, **29**, 2176–2179.
[32]   C. P. Gordon, C. Raynaud, R. A. Andersen, C. Copéret and O. Eisenstein, *Acc. Chem. Res.*, 2019, **52**, 2278–2289.
[33]   C. M. Widdifield and R. W. Schurko, *Concepts Magn. Reson. Part A*, 2009, **34A**, 91–123.

Author contributions